Phase field modeling of fracture in Functionally Graded Materials: Γ-convergence and mechanical insight on the effect of grading

Phase field modelling of fracture in Functionally Graded Materials: Γ-convergence and mechanical insight on the effect of grading

P K Asur Vijaya Kumar[a,*], A. Dean[b,c], J. Reinoso[c], P. Lenarda[a], M. Paggi[a]

[a] *IMT School for Advanced Studies Lucca, Piazza San Francesco 19, 55100, Lucca, Italy*
[b] *Institute of Structural Analysis, Leibniz Universität Hannover, Appelstr. 9A, 30167 Hannover, Germany*
[c] *Elasticity and Strength of Materials Group, School of Engineering, Universidad de Sevilla, Camino de los Descubrimientos s/n, 41092, Seville, Spain*

Abstract

A phase field (PF) approximation of fracture for functionally graded materials (FGM) using a diffusive crack approach incorporating the characteristic length scale as a material parameter is herein proposed. A rule of mixture is employed to estimate the material properties, according to the volume fractions of the constituent materials, which have been varied according to given grading profiles. In addition to the previous aspects, the current formulation includes the internal length scale of the phase field approach variable from point to point, to model a spatial variation of the material strength. Based on the ideas stemming from the study of size-scale effects, Γ-convergence for the proposed model is proved when the internal length scale is either constant or a bounded function. In a comprehensive sensitivity analysis, the effects of various model parameters for different grading profiles are analyzed. We first prove that the fracture energy and the elastic energy of FGM is bounded by their homogeneous constituents. Constitutive examples of boundary value problems solved using the BFGS solver are provided to bolster this claim. Finally, crack propagation events in conjunction with the differences with respect to their homogeneous surrogates are discussed through several representative applications, providing equivalence relationships for size-scale effects and demonstrating the applicability of the current model for structural analysis of FGMs.

Keywords: Fracture mechanics; Γ-Convergence; Phase Field; Functionally Graded Materials; Finite Element Method

1. Introduction

Mismatch in the material properties of mechanical components generally leads to the occurrence of weak interfaces which induce abnormal stress concentrations, and eventually leading to failure. In order to prevent such phenomena, the concept of Functionally Graded Materials (FGM), i.e. materials with spatial composition, has been intensively exploited in the last decades precluding interfacial stress concentration, and hence ameliorate resistance to failure [1]. Such a technological solution has attracted attention in the engineering community and industry so far [2]. In the recent past, FGMs have gained a notable popularity and have been applied in (but not limited to) turbine blades [3], rocket engines [4], artificial bone implants [5], shell structures [6] and airplanes [1].

Various studies [7, 8] have shown that FGMs are fundamentally different from homogeneous materials, and hence their corresponding crack propagation behavior can be especially complex [9]. There are multitude of factors affecting the crack growth of FGMs including: the ratio of Young's modulii [10], intrinsic toughness, strength variations [11], geometry, residual stresses, grading laws, among many other aspects. These factors

*Corresponding authors
Email address: pavan.asur@imtlucca.it (P K Asur Vijaya Kumar)

suggest that any predictive model for crack events in FGM should incorporate the intrinsic variation of material properties according to its grading profile.

Cracks oriented perpendicular to the grading profile experiences asymmetric loading at the crack tip and crack propagation may change its direction leading to mode-mixity, which in turn alters the stress intensity [12, 13], while grading parallel to cracks leads to straight propagation [11]. The effective composite properties of FGM generally vary in a continuous manner within the specimen domain as a combination of its homogeneous constituents [9, 14]. Introduction of the continuous grading alters the stress field, leading to modified stress intensity factors and mode mixity. Moreover, in this context, several studies revealed that spatial variation in the toughness and in the yield strain [15, 16, 9] meant that the failure stress/strain values at any point might depend on the grading. These factors inevitably restricts the study of cracks in FGM using conventional numerical methods and hence their general behavior with respect to crack propagation.

Derived from the previous complex response, computational methods such as the finite element methods (FEM) have been extensively used in the literature for exploring fracture in FGM and linear elastic fracture mechanics, see [17, 18, 19]. Early investigation of mixed-mode cracks within the context of FEM can be seen in [20]. Gu et al. [21] used domain integral technique to simplify the model for calculating crack tip field for FGM. Anlas et al. [22] estimated stress-intensity factors in FGM using FEM by assigning different homogeneous properties to each element. Bao et al. [23] studied multiple cracking in FGM coatings. Kim and paulino [24] developed and implemented general purpose FEM formulation considering mixed-mode cracks. Discrete numerical methods are widely used in the study of crack propagation phenomena such as XFEM [25, 26, 27], scaled boundary FE formulation [28], re-meshing algorithms based on cohesive elements (relying on the cohesive zone model, CZM) [29, 30], isoparametric graded finite element formulation [31, 32, 33]. Recently, Hrishikesh et al. [34] explored the possibility to simulate fracture events in FGMs using the phase field (PF) approach for fracture due to its strong potential (especially for composite structures [35, 36, 37, 38] and heterogeneous media [39, 40, 41, 42, 43, 44, 45, 46]) and partially verified the results with the experimental evidence. In this direction, recent studies concerned dynamic crack propagation in FGM using the phase field method [47, 48], and meshfree methods [49], showing a tremendous potential, and providing a plausible route for the thorough treatment of dynamic simulations.

In contrast to previous studies, in this investigation, we propose an extension of the phase field model for fracture in [34] by considering the internal characteristic length scale as a intrinsic material parameter. In this regard, first, we carefully analyze that for any given bounded characteristic length scale (not limited to FGM), proving that the total energy Γ-converges to the Griffith's theory under the size-scale effects using the mathematical setting as derived in [50]. Also, we gain a further insight into the general mechanical properties of FGM which can be used to analyze, create or modify future design of FGMs. Due to the underpinned internal length scale, the difference in the failure strain at any material point is addressed in line with [34, 9, 13]. These ingredients yield to a novel PF crack method for FGMs which provides a further potential for the exploration of the different aspects of the characteristic material and length scale properties onto the overall cracking response of the specimen.

The manuscript is organized as follows. In Section 2, the main aspects of the modeling framework to simulate crack propagation in FGMs are presented by considering the internal length scale calculated using the spatial variation of the FGM composition. Section 3 provides the results of Γ-converges by constructing a sequence of minimisers such that the sequence of functionals converges to the Griffith's potential. In Section 4, we discuss the finite element implementation of the proposed model using Broyden-Fetcher-Goldfard–shanno (BFGS) algorithm in `ABAQUS` using `UEL` module. Section 5 presents several representative examples starting with the validation experiment. In the sequel, mechanical insights for the effect of grading is explored, whereby we first prove that the bulk energy and surface energy of the FGM is bounded between those of its homogeneous constituents. Subsequently, we address the issue of crack propagation, the effects of Young modulus on cracking response, apparent strength values, grading profile, initial crack length and position. An equivalence relationship based on size-scale effects is provided along with the examples so that the large models can be brought down to a smaller size to analyse them effectively and reduce computational efficiency. An application example for a single fiber-reinforced FGM matrix is explored to further assess the potential of the model for micromechanics.

2. Variational formulation

2.1. Phase field approximation

Let $\Omega \subset \mathbb{R}^{n_{dim}}$ ($n_{dim} = 1, 2, 3$ denotes spatial dimension) be an arbitrary solid body containing a functionally graded material in the n_{dim} Euclidean space $\mathbb{R}^{n_{dim}}$ with the crack set $\Gamma \subset \mathbb{R}^{n_{dim}-1}$. The body is characterized by the kinematic displacement field $\mathbf{u}(\mathbf{x})$ and the strain field is defined as a symmetric gradient $(\nabla^s(\cdot))$ of the displacement field $\boldsymbol{\varepsilon}(\mathbf{x}) := \nabla^s \mathbf{u}(\mathbf{x})$ for all $\mathbf{x} \in \Omega$. The external boundary $\partial\Omega \subset \mathbb{R}^{n_{dim}-1}$ is split into two disjoint sets, $\partial\Omega_{\mathbf{u}}$ and $\partial\Omega_t$, i.e $\partial\Omega_{\mathbf{u}} \cap \partial\Omega_t = \emptyset$ and $\overline{\partial\Omega_{\mathbf{u}} \cup \partial\Omega_t} = \partial\Omega$, such that displacement $\bar{\mathbf{u}}(\mathbf{x})$ for $\mathbf{x} \in \partial\Omega_{\mathbf{u}}$ and traction $\bar{\mathbf{t}}(\mathbf{x})$ for $\mathbf{x} \in \partial\Omega_t$ is applied as shown in the Figure 1. The external work $\mathcal{P}(\mathbf{u}(\mathbf{x}))$ due to the applied loading defined above is given by

$$\mathcal{P}(\mathbf{u}(\mathbf{x})) := \int_{\Omega} \boldsymbol{f_v} \cdot \mathbf{u} \, \mathrm{dV} + \int_{\partial\Omega_t} \bar{\mathbf{t}} \cdot \mathbf{u} \, \mathrm{dS}, \tag{1}$$

where $\boldsymbol{f_v} : \Omega \to \mathbb{R}^{n_{dim}}$ is the distributed body force.

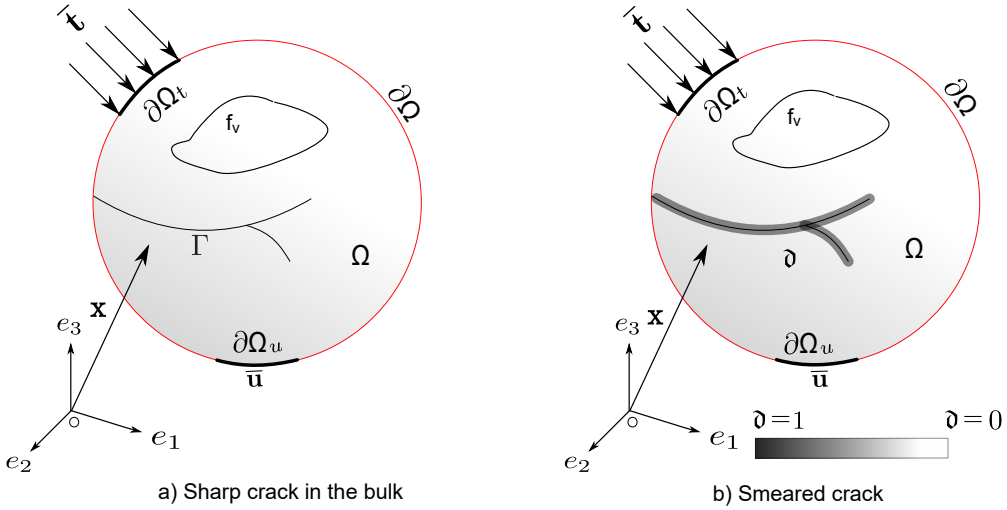

Figure 1: Schematic representation of diffusive cracks.

The variational approach to fracture according to Griffith's theory can be interpreted as the competition between the elastic energy $\Psi(\mathbf{u})$ created by the body due to external forces and the surface energy $\Psi_c(\Gamma)$ created by crack propagation. In this context, the quasi static displacement field $\mathbf{u}_t(\mathbf{x})$ and the crack set Γ_t at any given discrete time step $t \in [0, T]$ are given as a minimization problem (see [51] for more details)

$$(\mathbf{u}_t, \Gamma_t) = \arg\min \Pi(\mathbf{u}, \Gamma)_{\mathbb{S}} := \int_{\Omega \setminus \Gamma} \Psi(\boldsymbol{\varepsilon}) \, \mathrm{dV} + G_C \mathcal{H}^{n_{dim}-1}(\Gamma \cap \overline{\Omega} \setminus \partial\Omega_t), \tag{2}$$

with $\mathbb{S} := [\mathbf{u} = \bar{\mathbf{u}} \, \mathrm{on} \, \partial\Omega_{\mathbf{u}}, \, \Gamma_t \supset \Gamma_{t-1}]$, $\mathcal{H}^{n_{dim}-1}(\Gamma)$ is the Hausdorff $(n_{dim} - 1)$ dimensional measure of the unknown crack set Γ, G_C $[\mathrm{J}/m^2]$ is the critical energy release rate, and $\Psi(\boldsymbol{\varepsilon})$ is the elastic energy density that depends on the strain field $\boldsymbol{\varepsilon}(\mathbf{x})$.

Since Γ in Eq.(2) is unknown a priori, the numerical approximation of the functional given in the former expression is crafted as a free-discontinuity problem based on the Tortorelli's elliptical regularization [52] of the Mumford-Shah potential used in image segmentation [53], and later adapted to brittle fracture in [54, 51]. In this framework, the crack set Γ is replaced by $(\mathcal{H}^{n_{dim}-1}, n_{dim} - 1)$ rectifiable borel jump set of $\mathbf{u}$, $J(\mathbf{u})$. Then, there exists a sequence $(\Gamma_i)_i^{\infty}$ of C^1 hyper-surfaces, covering almost all of $J(\mathbf{u})$. ie $\mathcal{H}^1(J_u / \bigcup_{i=1}^{\infty} \Gamma_i) = 0$, in a suitable space such as $SBD(\Omega)/GSBD(\Omega)$ as detailed in Section 3, see [50, 55, 56]

for more details. Hence, the surface energy associated with the crack is approximated using a scalar field $\mathfrak{d} \in [0,1]$ (denominated as crack phase field variable), and the internal length scale $l \in \mathbb{R}^+$ governing the width of the diffusive crack such that, $\mathfrak{d} = 0$ for an intact material and $\mathfrak{d} = 1$ for completely damaged material takes the form, see Fig. 1

$$\Psi_c(\Gamma) = \int_\Gamma G_C \, \mathrm{dS} \approx \int_\Omega \frac{G_C}{4c_w} \gamma(\mathfrak{d}; \nabla\mathfrak{d}) \, \mathrm{dV}, \tag{3}$$

where, $\gamma(\mathfrak{d}; \nabla\mathfrak{d})$ is the crack surface energy density function [57] defined as

$$\gamma(\mathfrak{d}; \nabla\mathfrak{d}) := \frac{\alpha(\mathfrak{d})}{l} + l \left|\nabla\mathfrak{d}\right|^2. \tag{4}$$

Here, $c_w := \int_0^s \sqrt{\alpha(s)} ds$ is the normalization parameter, $\alpha(\mathfrak{d}) := \mathfrak{d}^2$ is the continuous monotonic function with $\alpha(0) = 0$ and $\alpha(1) = 1$, called as geometric crack function which determines the distribution of the phase field in line with AT-2 model [58, 59, 60]. The term $\frac{\alpha(\mathfrak{d})}{l}$ is local part, and $l\left|\nabla\mathfrak{d}\right|^2$ is the non-local part, which incorporates the internal length scale l. Due to the regularization of the crack Γ by the phase field variable $\mathfrak{d}$, the elastic energy now not only depends on the displacement field $\mathbf{u}(\mathbf{x})$, but also on the variable $\mathfrak{d}(\mathbf{x})$ as

$$\Psi(\mathbf{u}, \mathfrak{d}) = \int_\Omega g(\mathfrak{d}) \Psi_0(\boldsymbol{\varepsilon}(\mathbf{u})) \, \mathrm{dV}, \tag{5}$$

where $g(\mathfrak{d})$ is the energetic degradation function characterized by the deterioration of the initial elastic energy function $\Psi_0(\boldsymbol{\varepsilon})$ defined as $g(\mathfrak{d}) = (1-\mathfrak{d})^2 + K_l$, with $g(0) = 1$, $g(1) = 0$, $\frac{dg}{d\mathfrak{d}} < 0$, and $K_l = O(l)$. Since $\mathfrak{d}$ is bounded, the degradation function $g(\mathfrak{d}) = (1-\mathfrak{d})^2$ which maps $g(\mathfrak{d}) : [0,1] \to [1,0]$ is also bounded. Hence, the stored energy functional in Eq. (5) describes the transition from the intact state to the fully damaged state.

Thus, the total regularized energy functional of the solid in Eq. (2) takes the form:

$$\begin{aligned} \Pi_l(\mathbf{u}, \Gamma) = \int_\Omega \left[g(\mathfrak{d}) + K_l\right] \Psi(\boldsymbol{\varepsilon}) \, \mathrm{dV} + \int_\Omega \frac{G_C}{4c_w} \left[\frac{\alpha(\mathfrak{d})}{l} + l\left|\nabla\mathfrak{d}\right|^2\right] \, \mathrm{dV} \\ - \int_\Omega \boldsymbol{f_v} \cdot \mathbf{u} \, \mathrm{dV} - \int_{\partial\Omega} \bar{\mathbf{t}} \cdot \mathbf{u} \, \mathrm{dS}. \end{aligned} \tag{6}$$

The choice of $\alpha(\mathfrak{d})$ is motivated [57] by the fact that quadratic function for $\alpha(\mathfrak{d})$ ensures the admissible range $\mathfrak{d} \in [0,1]$ with an infinite support. As a consequence, the phase field should be solved in the whole computational domain. However, the high computational time due to finer mesh size in order to resolve the gradients in the phase field is overcome by creating external localized band on the crack path.

The elastic energy function given above is defined as $\Psi(\boldsymbol{\varepsilon}) = \boldsymbol{\varepsilon}(\mathbf{u})^T : \mathbb{C} : \boldsymbol{\varepsilon}(\mathbf{u})$, where $\mathbb{C}$ is the constitutive tensor relating stresses and strains.

2.2. Extension to Functionally Graded Materials

In the context of FGMs, it is evident that the the material properties exhibit a spatial variation within the specimen domain, and therefore they are functions of the material point [61, 62], i.e. depending on the location. Consider a FGM with grading profile $V_f = V_f(\mathbf{x})$ as a function of spatial variable $\mathbf{x}$. Then all the material properties can be expressed as a function of $V_f(\mathbf{x})$ i.e $G_C = G_C(\mathbf{x}, V_f) = G_C(\mathbf{x})$ and the compliance tensor $\mathbb{C} = \mathbb{C}(\mathbf{x}, V_f) = \mathbb{C}(\mathbf{x})$. The compliance tensor for the 2D plane strain takes the form:

$$\mathbb{C}(x) = \frac{E(\mathbf{x})}{(1+\nu(\mathbf{x}))(1-2\nu(\mathbf{x}))} \begin{bmatrix} 1-\nu(\mathbf{x}) & \nu(\mathbf{x}) & 0 \\ \nu(\mathbf{x}) & 1-\nu(\mathbf{x}) & 0 \\ 0 & 0 & \frac{1-2\nu(\mathbf{x})}{2} \end{bmatrix},$$

where $E(\mathbf{x})$ and $\nu(\mathbf{x})$ is the position-dependent Young's modulus and Poisson ratio respectively. See Section 5 for a complete set of examples.

As an example, for $n_{dim} = 2$, and $\mathbf{x} = [x, y]$ within a rectangular plate of width $2w$ and height $2b$, and grading in the y-direction, the volume fraction V_f of the material A can be defined as $V_f(\mathbf{x}) = \left(\frac{1}{2} + \frac{y}{h}\right)^K$, where K represent a material gradient index.

Then, via the invocation of the rule of mixtures, the Young's modulus at a generic point $\mathbf{x}$ as $E(\mathbf{x}) = E_A + (E_B - E_A)V_f(\mathbf{x})$, where E_A, E_B are the Young's modulus of material A and material B, respectively. Similarly, the fracture toughness K_{IC} and the Poisson ratio ν are expressed as $K_{IC}(\mathbf{x}) = K_{ICA} + (K_{ICB} - K_{ICA})V_f(\mathbf{x})$ and $\nu(\mathbf{x}) = \nu_A + (\nu_B - \nu_A)V_f(\mathbf{x})$ and hence the fracture energy for plane strain condition takes the form $G_{IC}(\mathbf{x}) = \frac{\left(1-\nu(\mathbf{x})^2\right)K_{IC}^2(\mathbf{x})}{E(\mathbf{x})}$.

The internal length scale l is largely considered as a material parameter [63]. This length scale l was experimentally determined in [64] for homogeneous materials, relating its value to the apparent material strength. Once the material parameter such as Young's modulus E , fracture toughness G_C are known, then the failure stress σ_c can be obtained using the closed-form relation $\sigma_c = \sqrt{G_C E/L}$, where L is the characteristics size of the specimen. In particular, Tanné and co-authors [65] proposed that, once these material properties are known, i.e $\sigma_c,\ E, G_C$, then the characteristic length l can be set as $l = \frac{27}{256}\left(\frac{G_{Ic}E}{\sigma_c^2}\right)$.

The rationale behind the choice of constant length scale in [34] is due to the intricate relation between critical stress σ_c and fracture toughness $K_{IC} = \sigma_c Y\sqrt{\pi a}$ where Y is a geometric factor and "a" is crack size. Under such conditions, the length scale given by $l = \frac{27}{256}\left(\frac{K_{IC}^2}{\sigma_c^2}\right) = \frac{27}{256}(Y^2\pi a)$ is a constant. However, within the context of FGM, this analysis can be assumed as simplification rendering the condition that the fracture toughness can be approximated as $K_{IC} = \sigma_\infty Y\sqrt{\pi a_c}$, where a_c is the smallest defect size, which in principle is an internal defect size depending upon the intrinsic material properties. Moreover, a general analysis might suggest that failure stress for FGM at different locations might also happen at different values, yielding that the critical stress σ_c required for cracking is also a function of grading. This later condition leads to approximate σ_c as a function of grading $V_f(\mathbf{x})$, and possibly the characteristics length scale l would be also a function of the spatial variation, i.e. function of the material point location $\mathbf{x}$. Thus, the variation of E, G_{Ic}, V_f on $\mathbf{x}$ suggests that each material point $\mathbf{x} \in \Omega$ has different characteristics, see [16] and the references therein. Accordingly, and without any loss of generality, we assume in the sequel that $\sigma_c = f(V_f)$ [65, 66]

$$l(\mathbf{x}) = \frac{27}{256}\left(\frac{G_{Ic}(\mathbf{x})E(\mathbf{x})}{\sigma_c^2(\mathbf{x})}\right). \tag{7}$$

Analyzing the previous expression, it is worth noting that the variation of length scale $l(\mathbf{x})$ depends on the elastic mismatch. For certain elastic mismatch, the variation of $l(\mathbf{x})$ can span across one order of magnitudes, as is discussed in the forthcoming Sections.

Consequently, the total energy functional of Eq.(6) in the context of FGM is given by

$$\Pi_{l(\mathbf{x})}(\mathbf{u}, \mathfrak{d}) = \int_\Omega \left[(1-\mathfrak{d})^2 + K_l\right](\Psi(\boldsymbol{\varepsilon}))\ \mathrm{dV} + \int_\Omega \frac{G_C(\mathbf{x})}{2}\left[\frac{\mathfrak{d}^2}{l(\mathbf{x})} + l(\mathbf{x})\left|\nabla\mathfrak{d}\right|^2\right]\ \mathrm{dV} - \int_\Omega \boldsymbol{f_v}\cdot\mathbf{u}\ \mathrm{dV} - \int_{\partial\Omega}\bar{\mathbf{t}}\cdot\mathbf{u}\,\mathrm{dS}, \tag{8}$$

with $\Psi(\boldsymbol{\varepsilon}) = \boldsymbol{\varepsilon}(\mathbf{u})^T : \mathbb{C}(\mathbf{x}) : \boldsymbol{\varepsilon}(\mathbf{u})$

Note that in order for the second integral in Eq.(8) to be mathematically meaningful, i.e [67, 68]

$$\int_\Omega \frac{G_C(\mathbf{x})}{2}\left[\frac{\mathfrak{d}^2}{l(\mathbf{x})} + l(\mathbf{x})\left|\nabla\mathfrak{d}\right|^2\right]\ \mathrm{dV} \in L^1(\Omega),$$

$G_C(\mathbf{x})$ and $l(\mathbf{x})$ has to be at least locally integrable functions, i.e $G_C(\mathbf{x}), l(\mathbf{x}) \in L^1_{loc}(\mathcal{A})$ in a compact set $\mathcal{A} \subset \Omega$ with $l(\mathbf{x}) \neq 0$ for all $\mathbf{x} \in \Omega$. It is easy to see that, if $V_f(\mathbf{x}) \in L^1_{loc}(\mathcal{A})$, then by construction $G_C(\mathbf{x}), l(\mathbf{x}) \in L^1_{loc}(\mathcal{A})$ for some compact set $\mathcal{A}$.

2.3. Governing equation in strong form

The solution to Eq. (8) can be obtained by solving it as a minimization problem, i.e determine $(\mathbf{u}, \mathfrak{d})$ from

$$(\mathbf{u}(\mathbf{x}),\, \mathfrak{d}(\mathbf{x})) = \arg\min_{\mathbf{x}} \{\Pi_{l(\mathbf{x})}(\mathbf{u}, \mathfrak{d})\}. \tag{9}$$

The governing (Euler-Lagrangian) equations under quasi-static conditions are determined by taking first variation of the functional $\Pi_{l(\mathbf{x})}(u, \mathfrak{d})$ in Eq. (8) in terms of Gateaux derivative for the variation $\delta\mathbf{u}$ and $\delta\mathfrak{d}$ of $\mathbf{u}$ and $\mathfrak{d}$ respectively, resulting in

$$\left[(1-\mathfrak{d})^2 + K_l\right] \nabla \cdot \boldsymbol{\sigma}(\mathbf{x}) + \boldsymbol{f_v}\mathbf{0} \quad \text{on } \Omega, \tag{10a}$$

$$\text{with } \boldsymbol{\sigma} \cdot \mathbf{n} = \bar{\mathbf{t}} \text{ on } \partial\Omega_t, \tag{10b}$$

$$G_C(\mathbf{x}) \left[\frac{\mathfrak{d}}{l(\mathbf{x})} - l(\mathbf{x})\boldsymbol{\Delta}\mathfrak{d}\right] - 2(1-\mathfrak{d})\Psi\left(\boldsymbol{\varepsilon}, \mathbf{x}\right) = 0 \text{ on } \Omega, \tag{10c}$$

$$\text{with } \nabla\mathfrak{d} \cdot \mathbf{n} = 0 \text{ on } \partial\Omega, \tag{10d}$$

where $\mathbf{n}$ is the outward normal vector on $\partial\Omega$. Note that on boundary, $\nabla\mathfrak{d} \cdot \mathbf{n} = 0$ and residual stiffness $K_l = 0$ because of compactness property [50, 52].

The unilateral stationary condition [51] of the total energy functional implies that $\delta\Pi_{l(\mathbf{x})} = 0$ for each $\delta\mathfrak{d}, \delta\mathbf{u} > 0$ and $\delta\Pi_{l(\mathbf{x})} > 0$ for $\delta\mathfrak{d},\ \delta\mathbf{u} = 0$, along with the irriversibility [51, 69] and boundedness of $\mathfrak{d}$ leads to the following first order optimality (KKT) conditions for the quasi-static evolution.

$$\dot{\mathfrak{d}} \geq 0, \tag{11a}$$

$$G_C(\mathbf{x}) \left[\frac{\mathfrak{d}}{l(\mathbf{x})} - l(\mathbf{x})\boldsymbol{\Delta}\mathfrak{d}\right] - 2(1-\mathfrak{d})\Psi(\boldsymbol{\varepsilon}, \mathbf{x}) \leq 0, \tag{11b}$$

$$\dot{\mathfrak{d}} \left\{G_C(\mathbf{x}) \left[\frac{\mathfrak{d}}{l(\mathbf{x})} - l(\mathbf{x})\boldsymbol{\Delta}\mathfrak{d}\right] - 2(1-\mathfrak{d})\Psi(\boldsymbol{\varepsilon}, \mathbf{x})\right\} = 0, \tag{11c}$$

where $\dot{\mathfrak{d}} = \frac{d\mathfrak{d}}{dt}$. The expression $G_C(\mathbf{x}) \left[\frac{\mathfrak{d}}{l(\mathbf{x})} - l(\mathbf{x})\boldsymbol{\Delta}\mathfrak{d}\right]$ indicates the energetic crack resistance and $2(\mathfrak{d} - 1)\Psi(\boldsymbol{\varepsilon})$ is the crack driving force.

3. Γ-Convergence analysis

As mentioned above, due to the bounded nature of $l(\mathbf{x})$, which may also involve non-linearity due to heuristic differences in the material properties, the Γ-convergence in the sense of [52, 50, 70] can still be applied under the assumption that the domain Ω is size-scaled.

We use the existing results in [50] and prove that the model in Eq. (6), under scaling in two dimension, mimics that of the AT-2 model with a little variation. Note that, it is possible to apply the more recent advancements as in [71, 55, 72] with small modifications, but we choose to use [50] because of the mechanical insight that can be derived from the L^∞ bounds on $\mathbf{u}(\mathbf{x})$.

In order for this proof to be self-consistent, we provide few important definitions and results, while further details can be seen in [50] and references therein which are omitted here for the sake of brevity. The proof is organised as follows, first we redefine the problem in terms of a scaling function, convert the total energy in terms of scaling which is similar to that of the classical AT-2 model. Using density and compactness results of the space $SBD(\Omega)$, we prove that the reduced energy functional satisfies lim-sup inequality by constructing a recovery sequence and later show that the results of [50] can be directly applied with small modification to get lim-inf inequality, if $l(\mathbf{x})$ is a bounded function (like in FGM) or even a constant (like in [73, 74])

3.1. Mathematical setting

Given $\mathbf{u} \in \Omega$, where Ω is open subset of $\mathbb{R}^{n_{dim}}$, one says displacement $\mathbf{u} : \Omega \to \mathbb{R}^{n_{dim}}$ has bounded deformation (BD), whenever the symmetric part of the distributional derivative $\boldsymbol{\varepsilon}(\mathbf{u}) = \left(\dfrac{D\mathbf{u} + D^T\mathbf{u}}{2}\right)$ is a bounded radon measure [56]. Moreover $\boldsymbol{\varepsilon}(\mathbf{u})$ can be decomposed into three parts, one absolutely continuous part with respect to Lebesgue measure $\mathrm{d}\mathbf{x}$, denoted by $\mathbf{e}(\mathbf{u})\mathrm{d}\mathbf{x}$, jump set carried by the rectifiable $(N-1)$ dimensional set J_u of points where the function $\mathbf{u}$ has approximate limits $\mathbf{u}^+(\mathbf{x})$ and $\mathbf{u}^-(\mathbf{x})$ together with some normal vector $\mathfrak{v}_u$ and Cantor part $\boldsymbol{\varepsilon}^c(\mathbf{u})$ which vanishes on Borel sets of finite $\mathcal{H}^{n_{dim}-1}$ measure. Meaning that, the crack set Γ (with respect to Lebesgue measure) is completely represented by the jump set J_u of $\mathbf{u}$. The space of $SBD(\Omega)$ (special function of bounded deformation) is defined as

$$SBD(\Omega) := \{\mathbf{u} \in BD(\Omega); \boldsymbol{\varepsilon}^c(\mathbf{u}) = 0\}.$$

Restricting the analysis to 2D case, i.e. $\Omega \subset \mathbb{R}^2$. Let $\bar{\boldsymbol{u}}$ be a position vector $\bar{\mathbf{u}} = [\bar{u}, \bar{v}]$ defined on Ω such that for all $\bar{\mathbf{u}} \in \Omega$, the kinematic displacement field in Ω be defined as $\mathbf{u}(\bar{\boldsymbol{u}}) = [u(\bar{\boldsymbol{u}}),\, v(\bar{\boldsymbol{u}})]$. Define the scaling function $S_\epsilon := \left(\dfrac{1}{2} + \dfrac{1}{2\epsilon}\right)$ and the continuous map $S_u : \Omega \to \Omega'$ with $S_u \in \mathbb{R}^{2\times 2}$ as

$$S_u := S_\epsilon \begin{bmatrix} 1 & 0 \\ 0 & 1 \end{bmatrix}. \tag{12}$$

Define the inverse mapping $S_u^{-1} : \Omega' \to \Omega$ as

$$S_u^{-1} := \frac{1}{S_\epsilon} \begin{bmatrix} 1 & 0 \\ 0 & 1 \end{bmatrix},$$

where $\epsilon > 0$ is a positive constant that goes to zero, and Ω' is the scaled domain such that $\Omega' = S_u\Omega \subset \mathbb{R}^2$. Let $\boldsymbol{x}$ be a position vector $\boldsymbol{x} := [x, y]$ defined on Ω', then for all $\boldsymbol{x} \in \Omega'$, $\boldsymbol{x}$ is defined in terms of scaling as $\boldsymbol{x} = S_u\,(\bar{\mathbf{u}})^T$. Meaning that

$$\boldsymbol{x} = [x, y] = S_\epsilon \begin{bmatrix} 1 & 0 \\ 0 & 1 \end{bmatrix} \begin{bmatrix} \bar{u} \\ \bar{v} \end{bmatrix} = S_\epsilon[\bar{u}, \bar{v}] = S_\epsilon \bar{\mathbf{u}}.$$

The corresponding displacement field on Ω' is defined as $\mathbf{u}(\boldsymbol{x})$. Assuming that each of the displacement field is bounded uniformly (by applied displacement) in $L^\infty(\Omega')$, for a fixed large enough applied displacement M', we have the following theorem.

Theorem 1. *Let Ω' be a Lipschitz-regular bounded open set. Let $M' > 0$, $\epsilon > 0$, for a positive bounded function $l(\boldsymbol{x}) \in L^1_{loc}(\Omega')$, define the functional for $(\mathbf{u},\, \mathfrak{d}) \in L^2(\Omega',\, \mathbb{R}^2) \times L^2(\Omega')$,*

$$\Pi_{l(\mathbf{x})}(\mathbf{u}, \mathfrak{d}) = \begin{cases} \int_{\Omega'} \left[(1-\mathfrak{d})^2 + K_\epsilon\right] \Psi(\mathbf{e}(\mathbf{u}))\; dV + \int_{\Omega'} \dfrac{G_C(\mathbf{x})}{2} \left[\dfrac{\mathfrak{d}^2}{l(\mathbf{x})} + l(\mathbf{x}) \left|\nabla \mathfrak{d}\right|^2\right]\; dV & \text{if } (\mathbf{u},\, \mathfrak{d}) \in H^1(\Omega',\, \mathbb{R}^2) \times \\ H^1(\Omega'),\ \text{and} \left\|u\right\|_{L^\infty} \le M' & \\ +\infty & \text{otherwise,} \end{cases} \tag{13}$$

with $K_\epsilon = o(\epsilon) \to 0$ as $\epsilon \to 0$. Then, as $\epsilon \to 0$, $\Pi_{l(\mathbf{x})}(u, \mathfrak{d})$ $\Gamma-$converges (in $L^2(\Omega',\, \mathbb{R}^2) \times L^2(\Omega')$) to

$$\Pi(\mathbf{u}, \mathfrak{d}) = \begin{cases} \int_\Omega \Psi(\mathbf{e}(\mathbf{u}))\; dV + G_C \mathcal{H}^1(J_u) & \text{if } \mathbf{u} \in SBD(\Omega),\ \mathfrak{d} = 1 \text{ and } \left\|u\right\|_{L^\infty} \le M' \\ +\infty & \text{otherwise} \end{cases}. \tag{14}$$

First, consider for all $\bar{\boldsymbol{u}} \in \Omega$, for displacement $\mathbf{u}(\bar{\boldsymbol{u}})$, it is assumed that $\mathbf{u}(\bar{\boldsymbol{u}}) \in SBD(\Omega)$, and is bounded by $\left\|\mathbf{u}\right\|_{L^\infty} \le M$. Then, it is easy to see that for all $\boldsymbol{x} \in \Omega'$, there exists a constant M' depending on the

scaling factor S_ϵ and M such that the deformation $\|\mathbf{u}\|_{L^\infty(\Omega')} \leq M'$. Hence, without loss of generality, we can assume that $\|\mathbf{u}\|_{L^\infty(\Omega')} \leq M'$ where M' is applied displacement on Ω'.

Physically, this means that, if body Ω with the applied displacement $M(\mathbf{u})$ produces a strain of $\boldsymbol{\varepsilon}(\mathbf{u})$, then, depending on the scaling factor S_ϵ, the same applied displacement $M(\mathbf{u})$ creates the strain proportional to $\dfrac{\boldsymbol{\varepsilon}(\mathbf{u})}{S_\epsilon}$ in Ω' (assuming uniform deformation). Hence, the applied displacement that is required to create the same strain $\boldsymbol{\varepsilon}(\mathbf{u})$ in Ω' depends on the scaling factor. To be precise $M' \propto S_\epsilon M$.

In [50], the compactness results for $\mathbf{u} \in SBD(\Omega)$ are shown in [Theorem 5.1, [50]]: If a sequence $(\mathbf{u}_n)_{n\geq 1}$ in $SBD(\Omega)$ is such that $\sup_{n\geq 1} \Pi_{l(\mathbf{x})}(\mathbf{u}, \Gamma) < \infty$, then up to a subsequence, there exists $\mathbf{u} \in SBD(\Omega)$ such that $\mathbf{u}_n \to \mathbf{u}$ strongly in $L^2(\Omega, \mathbb{R}^2)$, $\mathbf{e}(\mathbf{u}_n) \to \mathbf{e}(\mathbf{u})$ weakly in $L^2(\Omega; \mathbb{S}^{2\times 2})$ and $\mathcal{H}^{N-1}(J_u) \leq \liminf_{n\to\infty}(J_{u_n})$. Also, [Theorem 2, [50]] provides the density results for $\mathbf{u} \in SBD(\Omega) \cap L^2(\Omega, \mathbb{R}^2)$. Assuming $\sup_{n\geq 1} \Pi_{l(\mathbf{x})}(\mathbf{u}, \Gamma) < \infty$, then there exist a sequence $(\mathbf{u}_n)$ of displacement in $SBD(\Omega) \cap L^2(\Omega, \mathbb{R}^2)$, and $\|\mathbf{u}_n - \mathbf{u}\|_{L^2(\Omega,\mathbb{R}^2)} \to 0$, such that J_{u_n} is closed in Ω, contained in a finite union of closed connected pieces of C^1 curves, $\mathbf{u}_n \in H^1(\Omega/J_{u_n}; \mathbb{R}^2)$ and $\limsup_{n\to\infty} \Pi_{l(\mathbf{x})}(\mathbf{u}, \bar{J_{u_n}}) \leq \Pi_(\mathbf{u}, J_u)$.

With compactness and density results at hand, the proof of the Theorem 1 is organized as follows. First we show that Eq. (13), by a simple change of variable can be reduced to the energy potential function similar to that of the potential used in [50], but with a little difference. Later, we show the existence of minimizing sequence $(\mathbf{u}_\epsilon, \mathfrak{d}_\epsilon)$ to the reduced model so as to prove the lim-sup inequality. Later, we show that for the lim-inf inequality, the reduced model follows the same proof of lim-inf as in [50]. Due to the existence of minimizing sequence, and lim-sup inequality assuming a suitable coercivity property of the functional, the proof of the Theorem 1 is immediate.

3.2. Model reduction

Consider the energy functional in Eq. (13)

$$\Pi_{l(\mathbf{x})}(\mathbf{u}, \mathfrak{d}) = \int_{\Omega'} \left[(1-\mathfrak{d})^2 + K_\epsilon\right] \Psi(\mathbf{e}(\mathbf{u}))\, \mathrm{dV} + \int_{\Omega'} \frac{G_C(\mathbf{x})}{2} \left[\frac{\mathfrak{d}^2}{l(\mathbf{x})} + l(\mathbf{x}) \left|\nabla \mathfrak{d}\right|^2\right] \mathrm{dV},$$

notice that $\Omega' = S_u\Omega$ is the sizing domain which contains S_ϵ, the size-scaling factor. The choice of S_ϵ is motivated by the fact that when $\epsilon = 1$, $S_\epsilon = 1$ which coincide with the domain Ω. As $\epsilon \to 0$, Ω' expands and gives the same effect as if $l \to 0$ in Ω, meaning that as $\epsilon \to 0$, the surface energy asymptotically goes to the $\mathcal{H}^1(J_u)$ approaching a sharp crack.

Since, dealing with the expanding boundaries is mathematically challenging, by using simple change of variable, it is possible to move S_ϵ inside the integral. For this reason, consider the scaling as defined before $\boldsymbol{x} = S_\epsilon \bar{\mathbf{u}}$ implying $x = S_\epsilon \bar{u}$ and $y = S_\epsilon \bar{v}$.
From change of variable, we have

$$\int_{\Omega'} f(x,y) \mathrm{d}\boldsymbol{x} = \int_{\Omega} f(S_\epsilon \bar{u}, S_\epsilon \bar{v}) \left|\mathbf{J}\right| \mathrm{d}\bar{\mathbf{u}},$$

for the Jacobian,

$$|\mathbf{J}| = \frac{\partial(x,y)}{\partial(\bar{u},\bar{v})} = \begin{vmatrix} \dfrac{\partial x}{\partial \bar{u}} & \dfrac{\partial x}{\partial \bar{v}} \\ \dfrac{\partial y}{\partial \bar{u}} & \dfrac{\partial y}{\partial \bar{v}} \end{vmatrix} = \frac{\partial x}{\partial \bar{u}} \frac{\partial y}{\partial \bar{v}} = (S_\epsilon)^2 .$$

Now, the gradients can be defined as

$$\nabla \mathbf{u}(\boldsymbol{x}) = \left[\frac{\partial \mathbf{u}}{\partial x}, \frac{\partial \mathbf{u}}{\partial y}\right],$$

$$\frac{\partial \mathbf{u}}{\partial x} = \frac{\partial \mathbf{u}}{\partial \bar{u}} \frac{\partial \bar{u}}{\partial x} + \frac{\partial \mathbf{u}}{\partial \bar{v}} \frac{\partial \bar{v}}{\partial x} = \frac{\partial \mathbf{u}}{\partial \bar{u}} \frac{1}{S_\epsilon},$$

and

$$\frac{\partial \mathbf{u}}{\partial y} = \frac{\partial \mathbf{u}}{\partial \bar{u}}\frac{\partial \bar{u}}{\partial y} + \frac{\partial \mathbf{u}}{\partial \bar{v}}\frac{\partial \bar{v}}{\partial y} = \frac{\partial \mathbf{u}}{\partial \bar{v}}\frac{1}{S_\epsilon}.$$

Now, $\nabla \mathbf{u}(\boldsymbol{x}) = \dfrac{1}{S_\epsilon}\nabla \mathbf{u}(\bar{\mathbf{u}})$ where $\mathbf{u}(\bar{\mathbf{u}})$ is the displacement at scaled points. Notice that no assumption of the displacement is made here. Hence, we have $\boldsymbol{\varepsilon}(\mathbf{u}(\boldsymbol{x})) = \left(\dfrac{\nabla \mathbf{u} + \nabla^T \mathbf{u}}{2}\right) = \dfrac{1}{S_\epsilon}\boldsymbol{\varepsilon}(\mathbf{u}(\bar{\mathbf{u}}))$.

As in the case of the linear elasticity $\Psi(\boldsymbol{\varepsilon}(\mathbf{u})) = \boldsymbol{\varepsilon}(\mathbf{u}) : \mathbb{C}(\bar{\mathbf{u}}) : \boldsymbol{\varepsilon}(\mathbf{u})$, having a quadratic form and since $\mathbb{C}(\boldsymbol{x})$ is positive definite matrix, $\mathbb{C}(\bar{\mathbf{u}})$ is the continuous one to one mapping from Ω' to Ω without changing the matrix or its positive definiteness. From this, we can conclude that $\Psi(\boldsymbol{\varepsilon}(\mathbf{u}(\boldsymbol{x}))) = \dfrac{1}{S_\epsilon^2}\Psi(\boldsymbol{\varepsilon}(\mathbf{u}(\bar{\mathbf{u}})))$.

Now, the bulk energy becomes:

$$\int_{\Omega'} \left[(1-\mathfrak{d})^2 + K_\epsilon\right] \Psi(\mathbf{e}(\mathbf{u}))\mathrm{d}\boldsymbol{x} = \int_{\Omega} \left[(1-\mathfrak{d})^2 + K_\epsilon\right] \frac{1}{S_\epsilon^2}\Psi(\boldsymbol{\varepsilon}(\mathbf{u}(\bar{\mathbf{u}}))) \left|\mathbf{J}\right| \mathrm{d}\bar{\mathbf{u}} = \int_{\Omega} \left[(1-\mathfrak{d})^2 + K_\epsilon\right] \Psi(\boldsymbol{\varepsilon}(\mathbf{u}(\bar{\mathbf{u}}))) \mathrm{d}\bar{\mathbf{u}}.$$

Physically, this means that for a fixed applied displacement M', the bulk energy released by body Ω and Ω' are equal which can also be readily seen numerically in forthcoming analysis. Now consider the surface energy in Eq. (13),

$$\int_{\Omega'} \frac{G_C(\mathbf{x})}{2}\left[\frac{\mathfrak{d}^2}{l(\mathbf{x})} + l(\mathbf{x})\left|\nabla \mathfrak{d}\right|^2\right] \mathrm{d}\boldsymbol{x}.$$

In order to inherit the result of [50], it is required that $\mathfrak{d}^* = 1$ for intact material and $\mathfrak{d}^* = 0$ for fully broken state. Hence, renaming $\mathfrak{d}$, set $\mathfrak{d}^* = (1-\mathfrak{d})$, we have surface energy as

$$\int_{\Omega'} \frac{G_C(\mathbf{x})}{2}\left[\frac{\left(1-\mathfrak{d}^*\right)^2}{l(\mathbf{x})} + l(\mathbf{x})\left|\nabla \mathfrak{d}^*\right|^2\right] \mathrm{d}\boldsymbol{x}.$$

Applying change of variable here would result in

$$\int_{\Omega'} \frac{G_C(\mathbf{x})}{2}\left[\frac{\left(1-\mathfrak{d}^*\right)^2}{l(\mathbf{x})} + l(\mathbf{x})\left|\nabla \mathfrak{d}^*\right|^2\right] \mathrm{d}\boldsymbol{x} = \int_{\Omega} \frac{G_C(\mathbf{x})}{2}\left[\frac{\left(1-\mathfrak{d}^*(S_\epsilon\bar{\mathbf{u}})\right)^2}{l(\mathbf{x})}S_\epsilon^2 + l(\mathbf{x})\left|\nabla \mathfrak{d}^*(S_\epsilon\bar{\mathbf{u}})\right|^2\right] \mathrm{d}\bar{\mathbf{u}}.$$

Without loss of generality, relabeling and renaming the variables leads to

$$\int_{\Omega'} \frac{G_C(\mathbf{x})}{2}\left[\frac{\left(1-\mathfrak{d}^*\right)^2}{l(\mathbf{x})} + l(\mathbf{x})\left|\nabla \mathfrak{d}^*\right|^2\right] \mathrm{d}\boldsymbol{x} = \int_{\Omega} \frac{G_C(\mathbf{x})}{2}\left[\frac{\left(1-\mathfrak{d}^*\right)^2}{l(\mathbf{x})}S_\epsilon^2 + l(\mathbf{x})\left|\nabla \mathfrak{d}^*\right|^2\right] \mathrm{d}\boldsymbol{x}. \tag{15}$$

Combining bulk energy and surface energy leads to

$$\Pi_{l(\mathbf{x}),\epsilon}(\mathbf{u},\mathfrak{d}^*) = \int_{\Omega} \left[\mathfrak{d}^{*2} + K_\epsilon\right] \Psi(\boldsymbol{\varepsilon}(\mathbf{u}))\,\mathrm{d}\boldsymbol{x} + \int_{\Omega} \frac{G_C(\mathbf{x})}{2}\left[\frac{\left(1-\mathfrak{d}^*\right)^2}{l(\mathbf{x})}S_\epsilon^2 + l(\mathbf{x})\left|\nabla \mathfrak{d}^*\right|^2\right] \mathrm{d}\boldsymbol{x}, \tag{16}$$

with $\|\mathbf{u}\|_{L^\infty} \leq M'$, $\mathfrak{d}^* = 0$ for fully broken state and $\mathfrak{d}^* = 1$ for intact state and $\mathfrak{d}^* : \Omega \to [0,1]$.

Now, it becomes clear identify that functional in Eq. (13) and Eq. (16) are equivalent to each other. Also, this equivalence has an important consequence as an engineering application which is explained in Section 5.3.3. With the results on $SBD(\Omega)$ and L^∞ bounds on $\mathbf{u}$, Theorem 1 is equivalent to showing the $\Gamma-$convergence to the following Theorem

Theorem 2. *Let Ω be a lipschitz-regular bounded open set. Let $M' > 0$, $\epsilon > 0$, for a positive bounded function $l(\boldsymbol{x}) \in L^1_{loc}(\Omega)$, define the functional for $(\mathbf{u},\, \mathfrak{d}^*) \in L^2(\Omega,\, \mathbb{R}^2) \times L^2(\Omega)$,*

$$\Pi_{l(\mathbf{x}),\epsilon}(\mathbf{u}, \mathfrak{d}^*) = \begin{cases} \int_\Omega \left[\mathfrak{d}^{*2} + K_\epsilon\right] \Psi(\boldsymbol{\varepsilon}(\mathbf{u}))\, d\boldsymbol{x} + \int_\Omega \dfrac{G_C(\mathbf{x})}{2} \left[\dfrac{(1-\mathfrak{d}^*)^2}{l(\mathbf{x})} S_\epsilon^2 + l(\mathbf{x}) \left|\nabla \mathfrak{d}^*\right|^2\right] d\boldsymbol{x} & \text{if } (\mathbf{u},\, \mathfrak{d}^*) \in H^1(\Omega,\, \mathbb{R}^2) \times \\ H^1(\Omega) \text{ and } \|\mathbf{u}\|_{L^\infty} \leq M' & \\ +\infty & \text{otherwise,} \end{cases} \tag{17}$$

with $K_\epsilon = o(\epsilon) \to 0$ as $\epsilon \to 0$. Then, as $\epsilon \to 0$, $\Pi_{l(\mathbf{x}),\epsilon}(\mathbf{u}, \mathfrak{d}^*)$ $\Gamma-$converges (in $L^2(\Omega,\, \mathbb{R}^2) \times L^2(\Omega)$) to

$$\Pi(\mathbf{u}, \mathfrak{d}^*) = \begin{cases} \int_\Omega \Psi(\mathbf{e}(\mathbf{u})) d\boldsymbol{x} + G_C \mathcal{H}^1(J_u) & \text{if } \mathbf{u} \in SBD(\Omega),\ \mathfrak{d}^* = 1 \text{ and } \|\mathbf{u}\|_{L^\infty} \leq M' \\ +\infty & \text{otherwise} \end{cases}. \tag{18}$$

Proof. First notice that mechanical energy is the same in both Eq. (13) and (17) , also recall that J_u is $\left(\mathcal{H}^1, 1\right)$ rectifiable. Because of Theorem 3 of [50], we just need to prove lim-inf inequality for $(\mathbf{u}, \mathfrak{d}^*)$ with $\mathfrak{d}^* = 0$ and $\mathbf{u} \in SBD(\Omega)$ with $\mathcal{H}^1(\bar{J}_u) < \infty$, replacing $\mathcal{H}^1(J_u)$ by $\mathcal{H}^1(\bar{J}_u)$ in the energy (also assuming the closure of J_u, i.e $\bar{J}_u$ is rectifiable). Define distance function

$$d(\boldsymbol{x}) := \operatorname{dist}(\boldsymbol{x}, \bar{J}_u).$$

The volume of the area bounded by s-level set of d is

$$\boldsymbol{l}(s) = \left|\left\{\boldsymbol{x} \in \mathbb{R}^2;\, d(\boldsymbol{x}) \leq s\right\}\right| \text{ for all } s > 0.$$

The distance function is 1-lipshitz, i.e $|\nabla d(\boldsymbol{x})| = 1$ a.e. Now the co-area formula for lipshitz functions is given by

$$\boldsymbol{l}(s) = \int_0^s \mathcal{H}^1(\{\boldsymbol{x};\, d(\boldsymbol{x}) = t\}) \mathrm{d}t,$$

so that, in particular we have that

$$\boldsymbol{l}'(s) = \mathcal{H}^1(\{\boldsymbol{x};\, d(\boldsymbol{x}) = s\}).$$

Now, we can easily see that

$$\lim_{s \to 0} \frac{\boldsymbol{l}(s)}{s} = \lim_{s \to 0} \int_0^s \mathcal{H}^1(\{\boldsymbol{x};\, d(\boldsymbol{x}) = t\}) \mathrm{d}t = \mathcal{H}^1(\bar{J}_u),$$

as $s \to 0$, $d(\boldsymbol{x}) \to 0$ much faster than s itself and hence $\dfrac{\boldsymbol{l}(s)}{s}$ shrinks to $\mathcal{H}-$measure. i.e

$$\lim_{s \to 0} \frac{\boldsymbol{l}(s)}{s} = \mathcal{H}^1(\bar{J}_u).$$

The proof of the Lim-inf inequality result is mostly now standard [75, 76, 77] and Chambolle el at. [50] proved the result for linear elasticity. Hence, we show that the functional in Eq. (17) reduces to the already proven results and sketch the proof afterwards.

Consider a sequence $(\mathbf{u}_\epsilon, \mathfrak{d}^*_\epsilon)$ that converges to $(\mathbf{u}, \mathfrak{d}^*)$ such that $\sup_{\epsilon \geq 1} \Pi_{l(\mathbf{x}),\epsilon}(\mathbf{u}_\epsilon, \mathfrak{d}^*_\epsilon) < \infty$, then it is easy to show by taking for each ϵ a level set with $s_\epsilon \simeq 1/2$ such that $\sup_{\epsilon > 0} \mathcal{H}^1\left(\partial_* \left\{\mathfrak{d}^*_j > s\right\}\right) < \infty$, then there exists a sub-sequence $(\mathbf{u}_{\epsilon_j}, \mathfrak{d}^*_{\epsilon_j})$ converges to some $(\mathbf{u}, \mathfrak{d}^*)$ in $L^2(\Omega)$ as $\epsilon_j \to 0$(or $j \to \infty$) such that $\sup_{j \geq 1} \Pi_{l(\mathbf{x}),\epsilon}(\mathbf{u}_{\epsilon_j}, \mathfrak{d}^*_{\epsilon_j}) < \infty$. First note that, we must have $\mathfrak{d}^* = 1$, and consider the surface energy functional, and apply young's inequality in $L^2(\Omega)$ with $a^2 = \dfrac{(1-\mathfrak{d}^*)^2}{l(\mathbf{x})} S_\epsilon^2$, $b^2 = l(\mathbf{x}) \left|\nabla \mathfrak{d}^*\right|^2$ and $2ab \leq a^2 + b^2$, we have

$$\int_\Omega \left[\frac{\left(1-\mathfrak{d}_j^*\right)^2}{l(\mathbf{x})} S_{\epsilon_j}^2 + l(\mathbf{x}) \left|\nabla \mathfrak{d}_j^*\right|^2 \right] \mathrm{d}\boldsymbol{x} \geq \int_\Omega \left[\left|\left(1-\mathfrak{d}_j^*\right)\right| \left(1+\frac{1}{\epsilon_j}\right) \left|\nabla \mathfrak{d}_j^*\right| \right] \mathrm{d}\boldsymbol{x},$$

$$\geq \int_\Omega \left[\left|\left(1-\mathfrak{d}_j^*\right)\right| \left|\nabla \mathfrak{d}_j^*\right| \right] d\boldsymbol{x} + \int_\Omega \left[\left|\left(1-\mathfrak{d}_j^*\right)\right| \left(\frac{1}{\epsilon_j}\right) \left|\nabla \mathfrak{d}_j^*\right| \right] \mathrm{d}\boldsymbol{x},$$

$$\geq \int_\Omega \left[\left|\left(1-\mathfrak{d}_j^*\right)\right| \left|\nabla \mathfrak{d}_j^*\right| \right] \mathrm{d}\boldsymbol{x},$$

so that, using the co-area formula, we obtain

$$\Pi_{l(\mathbf{x}),\epsilon_j}(\mathbf{u}_j, \mathfrak{d}_j^*) \geq \int_0^1 \mathrm{d}s \left(\int_{\left\{\mathfrak{d}_j^* > s\right\}} 2s\Psi(\boldsymbol{\varepsilon}(\mathbf{u}_j))\, d\boldsymbol{x} + (1-s)\mathcal{H}^1\left(\partial_* \left\{\mathfrak{d}_j^* > s\right\}\right) \right).$$

Here, $\left(\partial_* \left\{\mathfrak{d}_j^* > s\right\}\right)$ is the reduced boundary of the finite perimeter set $\left\{\boldsymbol{x};\, \mathfrak{d}_j^*(\boldsymbol{x}) > s\right\}$ as in [78, 56, 50]. We can adopt here the results of SBD case with uniform L^∞ bound on the $\mathbf{u}$ as in proof of [lemma 5.1 [50]], we have for almost each $s \in (0,1)$, we have that

$$\int_\Omega 2s\Psi(\boldsymbol{\varepsilon}(\mathbf{u}))\, \mathrm{d}\boldsymbol{x} + 2(1-s)\mathcal{H}^1(J_u) \leq \liminf_{\epsilon\to 0} \int_0^1 \mathrm{d}s \left(\int_{\left\{\mathfrak{d}_j^* > s\right\}} 2s\Psi(\boldsymbol{\varepsilon}(\mathbf{u}_j))\, d\boldsymbol{x} + (1-s)\mathcal{H}^1\left(\partial_* \left\{\mathfrak{d}_j^* > s\right\}\right) \right).$$

Integrating over s and using Fatou's lemma and pass to the limits, we have the lim-inf inequality. i.e

$$\Pi_{l(\mathbf{x})}(\mathbf{u}, \mathfrak{d}^*) \leq \liminf_{\epsilon\to 0} \Pi_{l(\mathbf{x}),\epsilon_j}(\mathbf{u}_j, \mathfrak{d}_j^*).$$

Now for the lim-sup inequality, we construct a sequence $(\mathbf{u}_\epsilon, \mathfrak{d}_\epsilon^*)$ which converge in L^2 to $(\mathbf{u}, \mathfrak{d}^*)$, meaning that there exists a sequence that can go upto the Griffith's energy potential. If the constructed sequence of minimizers converges to a minimum, and sequence of functional also converge to the minimum value of the functional, then the limit of the sequence functions of minimizing sequence also converges upto a subsequence.

Consider the following sequence of minimizers

$$\mathbf{u}_\epsilon(\boldsymbol{x}) = \begin{cases} \dfrac{d(\boldsymbol{x})}{\alpha_\epsilon}\mathbf{u}(\boldsymbol{x}) & \text{if } 0 \leq d(\boldsymbol{x}) \leq \alpha_\epsilon \\ \mathbf{u}(\boldsymbol{x}) & \text{Otherwise,} \end{cases} \tag{19}$$

$$\mathfrak{d}_\epsilon^*(\boldsymbol{x}) = \begin{cases} 0 & \text{if } 0 \leq d(\boldsymbol{x}) \leq \alpha_\epsilon \\ 1 - \dfrac{\epsilon}{\sqrt{2l(\boldsymbol{x})}} exp\left(-\dfrac{d(\boldsymbol{x})-\alpha_\epsilon}{\epsilon^2}\right) & \text{if } d(\boldsymbol{x}) \geq \alpha_\epsilon. \end{cases} \tag{20}$$

Clearly $\mathbf{u}_\epsilon(\boldsymbol{x}) \to \mathbf{u}$ in $L^2(\Omega)$ as $\epsilon \to 0$ i.e

$$\int_\Omega (\mathbf{u}_\epsilon - \mathbf{u})^2\, \mathrm{d}\boldsymbol{x} = \int_{0\leq d(\boldsymbol{x})\leq \alpha_\epsilon} \left(\frac{d(\boldsymbol{x})}{\alpha_\epsilon}\mathbf{u}(\boldsymbol{x}) - \mathbf{u}(\boldsymbol{x})\right)^2 \mathrm{d}\boldsymbol{x} + \int_{d(\boldsymbol{x})\geq \alpha_\epsilon} (\mathbf{u}(\boldsymbol{x}) - \mathbf{u}(\boldsymbol{x}))^2\, \mathrm{d}\boldsymbol{x} = 0,$$

meaning that $\|\mathbf{u}_\epsilon - \mathbf{u}\|_{L^2(\Omega)} = 0$.

Similarly, $\mathfrak{d}_\epsilon^*(\boldsymbol{x}) \to 1$ as $\epsilon \to 0$ almost everywhere since $\mathfrak{d}_\epsilon^* \leq 1$ and $\dfrac{\epsilon}{\sqrt{2l(\boldsymbol{x})}} \exp\left(-\dfrac{d(\boldsymbol{x})-\alpha_\epsilon}{\epsilon^2}\right) \to 0$ as $\epsilon \to 0$. Hence, we have that $\|\mathfrak{d}_\epsilon^* - \mathfrak{d}^*\|_{L^2(\Omega)} = 0$.
Now consider the bulk energy

$$\begin{aligned}\int_\Omega \left[\mathfrak{d}^{*2} + K_\epsilon\right] \Psi(\boldsymbol{\varepsilon}(\mathbf{u}))\,\mathrm{d}\boldsymbol{x} &\leq \int_{0(\boldsymbol{x})\leq\alpha_\epsilon} \left[\mathfrak{d}_\epsilon^{*2} + K_\epsilon\right] \Psi(\boldsymbol{\varepsilon}(\mathbf{u}_\epsilon))\,\mathrm{d}\boldsymbol{x} + \int_{d(\boldsymbol{x})\geq\alpha_\epsilon} \left[\mathfrak{d}_\epsilon^{*2} + K_\epsilon\right] \Psi(\boldsymbol{\varepsilon}(\mathbf{u}_\epsilon))\,\mathrm{d}\boldsymbol{x},\\ &\leq \int_{0\leq d(\boldsymbol{x})\leq\alpha_\epsilon} K_\epsilon \Psi(\boldsymbol{\varepsilon}(\mathbf{u}_\epsilon))\,\mathrm{d}\boldsymbol{x} + \int_{d(\boldsymbol{x})\geq\alpha_\epsilon} \left[1+K_\epsilon\right] \Psi(\boldsymbol{\varepsilon}(\mathbf{u}_\epsilon))\,\mathrm{d}\boldsymbol{x}.\end{aligned}$$

Note that for $d(\boldsymbol{x}) \leq \alpha_\epsilon$

$$\nabla\mathbf{u}_\epsilon(\boldsymbol{x}) = \frac{d(\boldsymbol{x})}{\alpha_\epsilon}\nabla\mathbf{u}(\boldsymbol{x}) + \frac{\nabla d(\boldsymbol{x})}{\alpha_\epsilon}\mathbf{u}(\boldsymbol{x}) \leq \frac{d(\boldsymbol{x})}{\alpha_\epsilon}\nabla\mathbf{u}(\boldsymbol{x}) + \frac{M'}{\alpha_\epsilon}.$$

Here, we used 1-Lipshitz characteristic of $d(\boldsymbol{x})$ and L^∞ bounds on the $\mathbf{u}$. With this it is immediate that as $\epsilon \to 0$, the volume of the integral between $0 \leq d(\boldsymbol{x}) \leq \alpha_\epsilon$ shrinks to zero and for $d(\boldsymbol{x}) \geq \alpha_\epsilon$,

$$\Psi(\boldsymbol{\varepsilon}(\mathbf{u}_\epsilon)) \leq \left(\frac{d(\boldsymbol{x})}{\alpha_\epsilon}\nabla\mathbf{u}(\boldsymbol{x})\right)^2 + \left(\frac{M'}{\alpha_\epsilon}\right)^2 + \frac{d(\boldsymbol{x})}{\alpha_\epsilon}\left|\nabla\mathbf{u}(\boldsymbol{x})\right|\frac{M'}{\alpha_\epsilon},$$

$$\begin{aligned}\int_\Omega \left[\mathfrak{d}^{*2} + K_\epsilon\right] \Psi(\boldsymbol{\varepsilon}(\mathbf{u}))\,\mathrm{d}\boldsymbol{x} \leq &\int_{0\leq d(\boldsymbol{x})\leq\alpha_\epsilon} K_\epsilon \left(\frac{d(\boldsymbol{x})}{\alpha_\epsilon}\right)^2 \Psi(\boldsymbol{\varepsilon}(\mathbf{u}_\epsilon))\,\mathrm{d}\boldsymbol{x} + \int_{0\leq d(\boldsymbol{x})\leq\alpha_\epsilon} K_\epsilon \left(\frac{M'}{\alpha_\epsilon}\right)^2 \mathrm{d}\boldsymbol{x}\\ &+ \int_{0\leq d(\boldsymbol{x})\leq\alpha_\epsilon} K_\epsilon \left(\frac{d(\boldsymbol{x})}{\alpha_\epsilon}\right)^2 M'\sqrt{\Psi(\boldsymbol{\varepsilon}(\mathbf{u}_\epsilon))}\,\mathrm{d}\boldsymbol{x} + \int_{d(\boldsymbol{x})\geq\alpha_\epsilon} \left[1+K_\epsilon\right] \Psi(\boldsymbol{\varepsilon}(\mathbf{u}_\epsilon))\,\mathrm{d}\boldsymbol{x}.\end{aligned}$$

Now as $\epsilon \to 0$, $\alpha_\epsilon = o(\epsilon) \to 0$ faster than ϵ. Setting $K_\epsilon = o(\alpha_\epsilon) \to 0$ faster than α_ϵ . So, $\dfrac{K_\epsilon}{\alpha_\epsilon} \to 0$, $\dfrac{d(\boldsymbol{x})}{\alpha_\epsilon} \to 0$ and

$$\int_{0\leq d(\boldsymbol{x})\leq\alpha_\epsilon} K_\epsilon \left(\frac{M'}{\alpha_\epsilon}\right)^2 \mathrm{d}\boldsymbol{x} = K_\epsilon \left(\frac{M'}{\alpha_\epsilon}\right)^2 \boldsymbol{l}(\alpha_\epsilon) \to 0.$$

With this, we can conclude that

$$\limsup_{\epsilon\to 0} \int_\Omega \left[\mathfrak{d}^{*2} + K_\epsilon\right] \Psi(\boldsymbol{\varepsilon}(\mathbf{u}))\,\mathrm{d}\boldsymbol{x} \leq \int_\Omega \Psi(\boldsymbol{\varepsilon}(\mathbf{u}))\,\mathrm{d}\boldsymbol{x}. \tag{21}$$

Similarly, consider the surface energy term without $G_C(\boldsymbol{x})$.

$$\int_\Omega \left[\frac{(1-\mathfrak{d}^*)^2}{2l(\mathbf{x})}S_\epsilon^2 + \frac{l(\mathbf{x})}{2}\left|\nabla\mathfrak{d}^*\right|^2\right] \mathrm{d}\boldsymbol{x} \leq \int_{0\leq d(\boldsymbol{x})\leq\alpha_\epsilon} \left[\frac{(1-\mathfrak{d}_\epsilon^*)^2}{2l(\mathbf{x})}S_\epsilon^2 + \frac{l(\mathbf{x})}{2}\left|\nabla\mathfrak{d}_\epsilon^*\right|^2\right] \mathrm{d}\boldsymbol{x} + \int_{d(\boldsymbol{x})\geq\alpha_\epsilon} \left[\frac{(1-\mathfrak{d}_\epsilon^*)^2}{2l(\mathbf{x})}S_\epsilon^2 + \frac{l(\mathbf{x})}{2}\left|\nabla\mathfrak{d}_\epsilon^*\right|^2\right] \mathrm{d}\boldsymbol{x}$$

For $d(\boldsymbol{x}) \geq \alpha_\epsilon$

$$\mathfrak{d}_\epsilon^* = 1 - \frac{\epsilon}{\sqrt{2l(\boldsymbol{x})}} exp\left(-\frac{d(\boldsymbol{x})-\alpha_\epsilon}{\epsilon^2}\right),$$

$$\left(\frac{1+\epsilon}{2\epsilon}\right)^2 |1-\mathfrak{d}_\epsilon^*|^2 = \frac{(1+\epsilon)^2}{2l(\boldsymbol{x})} exp\left(-\frac{d(\boldsymbol{x})-\alpha_\epsilon}{\epsilon^2}\right).$$

Calculating $|\nabla\mathfrak{d}_\epsilon^*|^2$, with a simple algebraic manipulation results in $l(\boldsymbol{x})\,|\nabla\mathfrak{d}_\epsilon^*|^2 \leq \frac{1}{2\epsilon^2} exp\left(-\frac{d(\boldsymbol{x})-\alpha_\epsilon}{\epsilon^2}\right)$. Putting this in the surface energy, we have

$$\begin{aligned}\int_\Omega \left[\frac{(1-\mathfrak{d}^*)^2}{2l(\mathbf{x})} S_\epsilon^2 + \frac{l(\mathbf{x})}{2}|\nabla\mathfrak{d}^*|^2\right] \mathrm{d}\boldsymbol{x} \leq & \int_{0\leq d(\boldsymbol{x})\leq\alpha_\epsilon} \frac{1}{2l(\mathbf{x})} S_\epsilon^2\,\mathrm{d}\boldsymbol{x} + \int_{d(\boldsymbol{x})\geq\alpha_\epsilon} \frac{(1+\epsilon)^2}{2l(\boldsymbol{x})} exp\left(-\frac{d(\boldsymbol{x})-\alpha_\epsilon}{\epsilon^2}\right)\mathrm{d}\boldsymbol{x} \\ & + \int_{d(\boldsymbol{x})\geq\alpha_\epsilon} \frac{1}{2\epsilon^2} exp\left(-\frac{d(\boldsymbol{x})-\alpha_\epsilon}{\epsilon^2}\right)\mathrm{d}\boldsymbol{x}.\end{aligned}$$

In this inequality, first term and second term goes to zero as $\epsilon \to 0$ is immediate. Consider the third term

$$\begin{aligned}\int_{d(\boldsymbol{x})\geq\alpha_\epsilon} \frac{1}{2\epsilon^2} exp\left(-\frac{d(\boldsymbol{x})-\alpha_\epsilon}{\epsilon^2}\right)\mathrm{d}\boldsymbol{x} &= \frac{1}{2\epsilon^2}\int_{d(\boldsymbol{x})\geq\alpha_\epsilon} exp\left(\frac{-s}{\epsilon^2}\right) exp\left(\frac{\alpha_\epsilon}{\epsilon^2}\right)\,\mathcal{H}^1(\{\,\mathrm{d}(\boldsymbol{x})=s\})\mathrm{d}\boldsymbol{x}, \\ &= \frac{1}{2\epsilon^2}\int_{d(\boldsymbol{x})\geq\alpha_\epsilon} exp\left(\frac{-s}{\epsilon^2}\right) exp\left(\frac{\alpha_\epsilon}{\epsilon^2}\right)\,\boldsymbol{l}'(s)\mathrm{d}\boldsymbol{x}.\end{aligned}$$

by setting $\frac{s}{\epsilon^2} := t$, changing the variable and integrating it by parts would result in

$$\int_{d(\boldsymbol{x})\geq\alpha_\epsilon} \frac{1}{2\epsilon^2} exp\left(-\frac{d(\boldsymbol{x})-\alpha_\epsilon}{\epsilon^2}\right)\mathrm{d}\boldsymbol{x} = \frac{\boldsymbol{l}'(\alpha_\epsilon)}{2} + \frac{e^{\left(\frac{\alpha_\epsilon}{\epsilon^2}\right)}}{2\epsilon^2}\int_{d(\boldsymbol{x})\geq\alpha_\epsilon} \left(\frac{\alpha_\epsilon}{\epsilon^2}+t\right)\frac{\boldsymbol{l}(\alpha_\epsilon+\epsilon^2 t)}{2\,(\alpha_\epsilon+\epsilon^2 t)} e^{-t}\mathrm{d}t.$$

Taking limit of the function as $\epsilon \to 0$ leads to

$$\limsup_{\epsilon\to 0}\int_\Omega \left[\frac{(1-\mathfrak{d}^*)^2}{2l(\mathbf{x})} S_\epsilon^2 + \frac{l(\mathbf{x})}{2}|\nabla\mathfrak{d}^*|^2\right]\mathrm{d}\boldsymbol{x} \leq \mathcal{H}^1(\bar{J}_u).$$

Combining both surface energy and bulk energy we have the lim-sup inequality.

i.e

$$\limsup_{\epsilon\to 0} \Pi_{l(\mathbf{x}),\epsilon}(\mathbf{u}_\epsilon, \mathfrak{d}_\epsilon^*) \leq \Pi(\mathbf{u}, \mathfrak{d}^*).$$

and hence the proof of Theorem 2. By equivalence relation as stated, we also have the proof of Theorem 1. □

4. Finite element formulation

In this section, the FE implementation of the multi-field displacement-phase field model proposed in Eqs. (10a) and (10c) is presented. In order to construct the numerical solution of the corresponding initial boundary value problem (IBVP), we consider the weak form of the former set of equations for the test functions $\delta\mathbf{u}$ and $\delta\mathfrak{d}$ of the primary fields $\mathbf{u}$, $\mathfrak{d}$ respectively:

$$\int_\Omega \left[(1-\mathfrak{d})^2 + K_l\right] \boldsymbol{\sigma} : \boldsymbol{\varepsilon}(\delta\mathbf{u}) \mathrm{dV} - \int_\Omega \boldsymbol{f_v} \delta\mathbf{u} \ \mathrm{dV} - \int_{\partial\Omega} \bar{\mathbf{t}} \delta\mathbf{u} \, \mathrm{dS} = 0,$$
$$\int_\Omega G_C(\mathbf{x}) \left[\frac{\mathfrak{d}}{l(\mathbf{x})}\delta\mathfrak{d} + l(x)\nabla\mathfrak{d}\cdot\nabla\delta\mathfrak{d}\right] \ \mathrm{dV} - \int_\Omega 2(1-\mathfrak{d})\Psi\left(\boldsymbol{\varepsilon},\mathbf{x}\right)\delta\mathfrak{d} \ \mathrm{dV} = 0.$$

Note that, it is often recommended to use unequal interpolation orders for the coupled multi-field problems in order to avoid stress oscillations and potential numerical interlocking. Notwithstanding, it can be argued from previous investigations [79, 80, 81] that this strategy is not required in the present study since the stress oscillations and numerical locking might only arise in a very narrow band of crack propagation and have negligible effects on the convergence rates and numerical results of the overall problem.

Accordingly, we define dicretization $\Omega \to \Omega_e$, $\mathbf{u} \to \mathbf{u}_e$, $\delta\mathbf{u} \to \delta\mathbf{u}_e$, $\mathfrak{d} \to \mathfrak{d}_e$, $\delta\mathfrak{d} \to \delta\mathfrak{d}_e$ such that $\mathbf{u}_e \in \mathcal{U}_h$, $v_e \in \mathcal{V}_h$, $\mathfrak{d}_e \in \mathcal{U}_\mathfrak{d}$, $\delta\mathfrak{d}_e \in \mathcal{U}_{\delta\mathfrak{d}}$, and partition of unity holds for the functional space for approximate functions

$$\mathcal{U}_h(\mathbf{u}) = \left\{ \mathbf{u} \in H^1(\Omega) \middle| \nabla\mathbf{u} \in L^2(\Omega);\, \mathbf{u} = \mathbf{u}_d \,\text{on}\, \partial\Omega_d \right\}, \tag{22a}$$
$$\mathcal{V}_h(\delta\mathbf{u}) = \left\{ \delta\mathbf{u} \in H^1(\Omega) \middle| \nabla\delta\mathbf{u} \in L^2(\Omega);\, \delta\mathbf{u} = 0 \,\text{on}\, \partial\Omega_d \right\}, \tag{22b}$$
$$\mathcal{U}_\mathfrak{d}(\mathfrak{d}) = \left\{ \mathfrak{d} \in H^1(\Omega) \middle| \mathfrak{d}(x) \in [0,1],\, \dot{\mathfrak{d}} \geq 0 \ \forall \mathbf{x} \in \Omega \right\}, \tag{22c}$$
$$\mathcal{U}_{\delta\mathfrak{d}}(\delta\mathfrak{d}) = \left\{ \delta\mathfrak{d} \in H^1(\Omega) \middle| \delta\mathfrak{d} \geq 0 \, \forall \mathbf{x} \in \Omega \right\}. \tag{22d}$$

Upon the above setting, the displacement field $\mathbf{u}_e$ and the strain field $\boldsymbol{\varepsilon}(\mathbf{u}_e)$ are interpolated in terms of the nodal displacements $\mathbf{d_u}$ as follows

$$\mathbf{u}_e(\mathbf{x}) \approx \mathbf{N}(\mathbf{x})\mathbf{d_u} \quad \nabla\mathbf{u}_e(\mathbf{x}) \approx \mathbf{B}(\mathbf{x})\mathbf{d_u}, \tag{23}$$

where $\mathbf{N}(\mathbf{x})$ is the matrix that arranges the shape functions associated with at the element in computational domain Ω_e, and $\mathbf{B}(\mathbf{x})$ identifies its corresponding spatial derivative (also denominated as compatibility operator).

In a similar manner, complying with an isoparametric formulation, the FE discretization of phase field $\mathfrak{d}$ variable and the gradient $\nabla\mathfrak{d}$ in terms of nodal phase field $\mathbf{d}_\mathfrak{d}$ renders

$$\mathfrak{d}_e(x) \approx \mathbf{N}(\mathbf{x})\mathbf{d}_\mathfrak{d} \quad \nabla\mathfrak{d}_e(x) \approx \mathbf{B}^\mathfrak{d}(\mathbf{x})\mathbf{d}_\mathfrak{d}, \tag{24}$$

where the same order of interpolation is chosen for the displacement and the phase field variables.

Through the insertion of the previous interpolation scheme for the displacement and the crack-like phase field variable, the discrete versions of the element residual vectors for both fields are given by

$$\mathbf{r_u} = \int_{\Omega_e} \left((1-\mathfrak{d})^2 + K_l\right) \mathbf{B}^\mathrm{T}(\mathbf{x})\boldsymbol{\sigma} \ \mathrm{dV} - \int_{\Omega_e} \mathbf{N}^\mathrm{T}(\mathbf{x})\boldsymbol{f_v} \ \mathrm{dV} - \int_{\partial\Omega_e} \mathbf{B}^\mathrm{T}(\mathbf{x})\bar{\mathbf{t}} \, \mathrm{dS}.$$
$$\mathbf{r}_\mathfrak{d} := \int_{\Omega_e} -2(1-\mathfrak{d})\mathbf{N}^\mathrm{T}(\mathbf{x})\Psi\left(\boldsymbol{\varepsilon},\mathbf{x}\right) \ \mathrm{dV} + \int_{\Omega_e} \frac{G_C(\mathbf{x})}{l(\mathbf{x})} \left[\mathbf{N}^\mathrm{T}\mathfrak{d} + l(\mathbf{x})^2(\mathbf{B}^\mathfrak{d})^T\nabla\mathfrak{d}\right] \ \mathrm{dV},$$

The solution is computed using quasi-newton solver. In line with [82, 83], the stiffness matrix is updated after each iteration according to Broyden-Fletcher-Goldfarb-Sahnno(BFGS) algorithm . In such case the initial guess for BFGS to estimate $(t+\Delta t)^{th}$ time step takes the form

$$\left[\begin{array}{c} \mathbf{d}_u \\ \mathbf{d}_\mathfrak{d} \end{array}\right]_{t+\Delta t} = \left[\begin{array}{c} \mathbf{d}_u \\ \mathbf{d}_\mathfrak{d} \end{array}\right]_t - \left[\begin{array}{cc} \mathbf{K_{uu}} & 0 \\ 0 & \mathbf{K}_{\mathfrak{d}\mathfrak{d}} \end{array}\right]_t^{-1} \left[\begin{array}{c} \mathbf{r_u} \\ \mathbf{r}_\mathfrak{d} \end{array}\right]_t. \tag{25}$$

Equivalently, we can express

$$(\mathbf{z})_{t+\Delta t} = (\mathbf{z})_t - \mathbf{K}_t^{-1}(\mathbf{r})_t \tag{26}$$

where

$$\frac{\partial \mathbf{R_u}}{\partial \mathbf{d}_u} = \mathbf{K_{uu}} = \int_{\Omega_e} \left((1-\mathfrak{d})^2 + K_l\right) \mathbf{B}^T \mathbb{C}(\mathbf{x}) \mathbf{B} \ \mathrm{dV}, \tag{27}$$

$$\frac{\partial \mathbf{R}_\mathfrak{d}}{\partial \mathbf{d}_\mathfrak{d}} = \mathbf{K}_{\mathfrak{d}\mathfrak{d}} = \int_{\Omega_e} 2\mathbf{N}^T\mathbf{N}\hat{\mathcal{H}} \ \mathrm{dV} + \int_{\Omega_e} \frac{G_C(\mathbf{x})}{l(\mathbf{x})} \left[\mathbf{N}^T\mathbf{N} + l(\mathbf{x})^2 (\mathbf{B}^\mathfrak{d})(\mathbf{B}^\mathfrak{d})^T\right] \ \mathrm{dV}. \tag{28}$$

are the elemental tangent stiffness matrix.

The above system of equations incorporates the history variable as in [84], denoted as $\hat{\mathcal{H}}$, in order to ensure irreversibility of the crack defined as

$$\hat{\mathcal{H}} = \max_{\tau \in [0,t]} (\Psi(t)). \tag{29}$$

The approximated stiffness matrix $\tilde{\mathbf{K}}$ is updated after a set number of iterations in case of not having an converged solution using

$$\tilde{\mathbf{K}} = \tilde{\mathbf{K}}_t - \frac{(\tilde{\mathbf{K}}_t \Delta \mathbf{z})(\tilde{\mathbf{K}}_t \Delta \mathbf{z})^T}{\Delta \mathbf{z} \tilde{\mathbf{K}}_t \Delta \mathbf{z}} + \frac{\Delta \mathbf{r} \Delta \mathbf{r}^T}{\Delta \mathbf{z}^T \Delta \mathbf{r}} \tag{30}$$

where $\Delta \mathbf{z} = \mathbf{z}_{t+\Delta t} - \mathbf{z}_t$, and $\Delta \mathbf{r} = \mathbf{r}_{t+\Delta t} - \mathbf{r}_t$. Therefore, that the approximated stiffness matrix $\tilde{K}$ satisfies

$$\tilde{\mathbf{K}} \Delta \mathbf{z} = \Delta \mathbf{r} \tag{31}$$

The system of equations has been implemented in finite element software `ABAQUS` in order to take advantage of the in-built BFGS solver. For this purpose, a user defined `UEL` is written for the coupled equilibrium equations. Moreover, with regard to the FGM formulation, the corresponding variation of material properties has been implemented at each material integration point in a continuous manner by fetching the data `COORDS(nnode, mcrd)` in abaqus `UEL` subroutine.

5. Numerical experiments

In this section, for validation purposes, a comprehensive numerical example of asymmetric three-point bending of PMMA beam is discussed. A qualitative assessment of crack path is performed, which is validated against available experimental results in order to show the predictive capabilities of the proposed model. Subsequently, using the classical benchmark problem of single-edge notched plate under tensile loading conditions, mechanical insights based on variation of Young's modulus ratio, initial crack length and position of the model are pinpointed, in conjunction with a final discussion on size-scale effects emphasizing the equivalence relationship. Finally, the current PF method for FGM is applied to study the failure initiation and propagation at the micro-scale in a single-fiber reinforced FGM matrix problem.

y(mm)	E_A(MPa)	ν	$K_{IC,A}$ (MPa$\sqrt{\text{m}}$)
0	1780	0.41	0.99
60	4000	0.39	1.19

Table 1: Material Properties of PMMA beam

5.1. Material properties/ grading

Let A and B are two material compositions of the functionally graded material with the volume fraction of Material A in the y-direction given as

$$V_f(\mathbf{x}) = \left(\frac{1}{2} + \frac{y}{h}\right)^K, \tag{32}$$

where K is a grading constant. The volume fraction of Material B can be estimated as $V_B(\mathbf{x}) = 1 - V_f(\mathbf{x})$. Based on the rule of mixtures, the corresponding Young's modulus, fracture toughness, Poisson ratio and apparent strength in terms of volume fractions takes the form:

$$E(\mathbf{x}) = E_1 + (E_2 - E_1)V_f(\mathbf{x}), \tag{33a}$$
$$K_{IC}(\mathbf{x}) = K_{1c,1} + (K_{1c,2} - K_{1c,1})V_f(\mathbf{x}), \tag{33b}$$
$$\nu(\mathbf{x}) = \nu_1 + (\nu_2 - \nu_1)V_f(\mathbf{x}), \tag{33c}$$
$$\sigma_c(\mathbf{x}) = \sigma_{c1} + (\sigma_{c2} - \sigma_{c1})V_f(\mathbf{x}). \tag{33d}$$

Assuming plain strain condition for all the numerical experiments, we have

$$G_C(\mathbf{x}) = \frac{(1-\nu(\mathbf{x})^2)K_{IC}(\mathbf{x})^2}{E(\mathbf{x})}, \quad l(\mathbf{x}) = \frac{27}{256}\left(\frac{G_C(\mathbf{x})E(\mathbf{x})}{\sigma_c^2(\mathbf{x})}\right). \tag{34}$$

All the material properties in the subsequent sections take the form as mentioned, unless specified.

5.2. Validation experiment

In this section, we investigate crack propagation in a graded PMMA beam subjected to three-point bending with unsymmetrical loading conditions. In this example, we consider the grading along the y-direction with the boundary condition shown in Figure 2. All the material properties are taken as the linear combination of the homogeneous properties in the grading direction according to the rule of mixtures as in Section 5.1. The material properties of the PMMA beam are listed in Table 1 in line with [85].

The domain is discretized with 97371 4-node quadrilateral plane stress elements. The length of each side of element near the process zone is kept less than 0.2 mm in order to ensure that gradient of the phase-field is resolved properly.

Fig. 3a shows the crack propagation path due to asymmetrical loading. Fig. 3b shows the comparison of the crack trajectories for the graded PMMA beam obtained by the present model and the experimental (averaged) results as in [85]. The crack propagation path due to the present model shows an excellent agreement with the experimental results. Moreover, Fig. 4 shows the comparison of the reaction force v/s displacement curve for the constant characteristic length scales of $l = 1.49$, $l = 2.51$ and the variable length scale $l(\mathbf{x})$. The results indicates that the small variation in the length scale affects the system behaviour which are reflected in the reaction force vs displacement curve (note that the grading profile chosen in this application is relatively smooth).

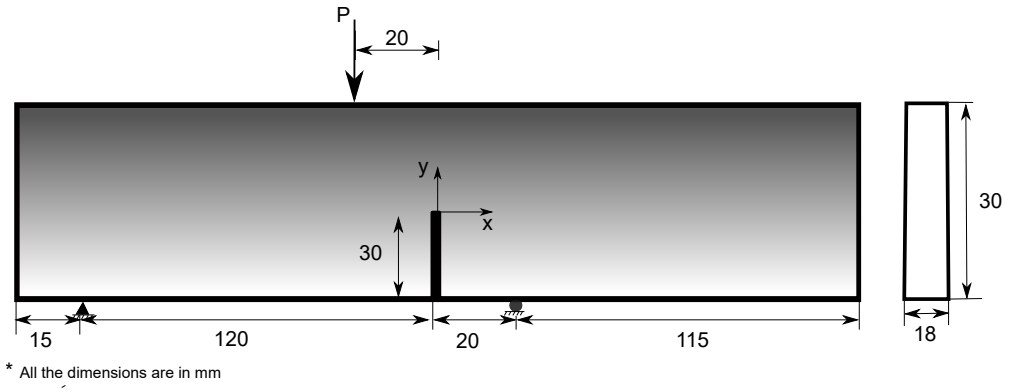

Figure 2: A crack in a beam subjected to three-point unsymmetrical loading

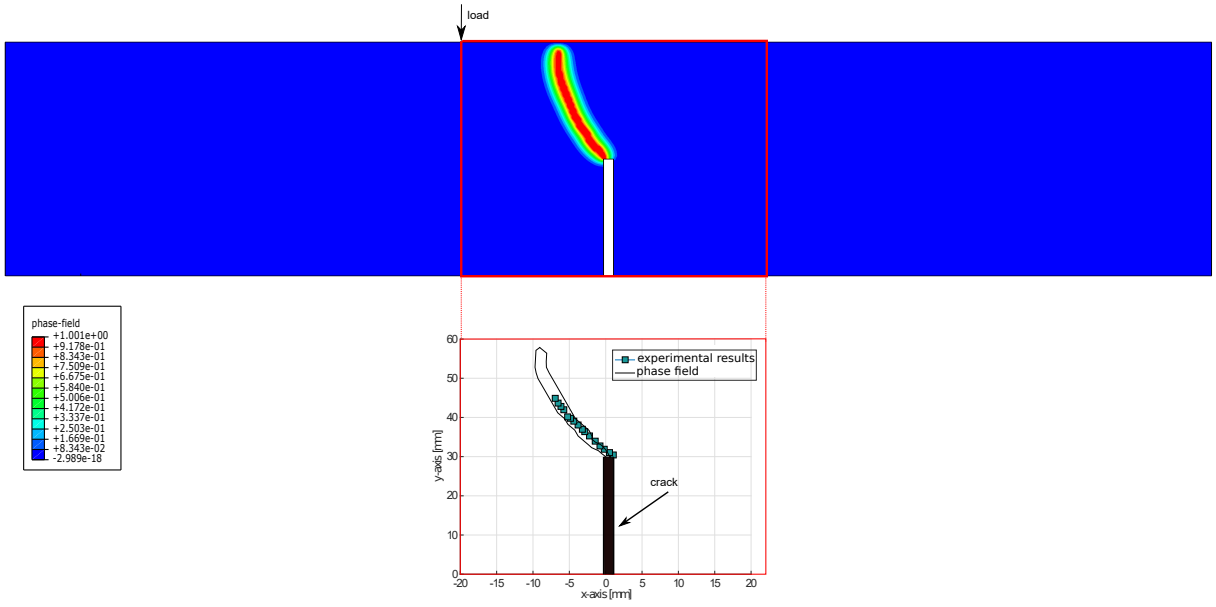

Figure 3: Crack propagation of PMMA beam under unsymmetrical loading condition. a)Crack propagation b)Comparison with experimental results.

5.3. Insights on the role of the different parameters of the formulation. Comprehensive analysis of grading profiles

In this section, we present several numerical examples which include a classical benchmark problem, corresponding a single-edge notched plate under monotonic tensile loading conditions up to failure. For each of the examples herein investigated, the effects of Young's modulus ratio, size effects, crack length and position effects, grading profiles on the crack propagation are pinpointed. Also, we provide a general behavior discussion on the response of FGM specimens using simple mathematical manipulations in order to support the numerical examples.

With the aim of understanding the effects of change of l at every material point, we invoke and recall the following theorem.

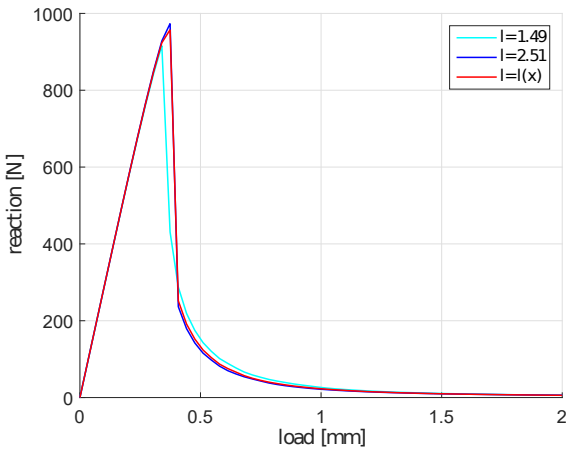

Figure 4: comparison between constant l and $l(\mathbf{x})$ for the reaction forces of asymmetrical three-point loading.

Theorem 3. *With the usual notations mentioned before, for every* $\mathbf{x} \in \mathbb{R}^{n_{dim}}$, *under the same domain* Ω *and loading conditions, for any given grading function* $V_f \in L^1_{loc}(\Omega)$,

1. Elastic energy $\Psi(\mathbf{u}, \mathfrak{d})$ *of FGM is comprised (bounded from above and below) between its homogeneous material composition. i.e*

$$\Psi(\mathbf{u}, \mathfrak{d})\Big|_{E_{min}} \leq \Psi(\mathbf{u}, \mathfrak{d}) \leq \Psi(\mathbf{u}, \mathfrak{d})\Big|_{E_{max}}.$$

2. Surface energy $\Psi_c(\mathfrak{d})$ *created due to fracture is bounded between its homogeneous material composition if the function* $f(x) = \frac{\sigma^2(\mathbf{x})}{E(\mathbf{x})}$ *is monotonic*

$$\Psi_c(\mathfrak{d})\Big|_{f(x)_{min}} \leq \Psi_c(\mathfrak{d}) \leq \Psi_c(\mathfrak{d})\Big|_{f(x)_{max}}.$$

Proof. **Part-1:** Let FGM has its constituents as Material A and B. Assume $E_A > E_B$, then for all $\mathbf{x} \in \Omega$, $V_f(\mathbf{x}) \in L^1_{loc}(\Omega)$ is a function such that, by construction

$$E_B = E_{min} \leq E(\mathbf{x}) \leq E_{max} = E_A \text{ meaning that } E(\mathbf{x}) \in [E_B, E_A].$$

Extending this inequality for the compliance tensor $\mathbb{C}(x)$ along with the fact that $\mathbb{C}(x)$ is positive definite[1] leads to

$$\mathbb{C}\Big|_{E_B} \leq \mathbb{C}(x) \leq \mathbb{C}\Big|_{E_A} \tag{35}$$

Consider the elastic energy of the FGM

$$\Psi(\mathbf{u}, \mathfrak{d}) = \int_\Omega \left[(1-\mathfrak{d})^2 + K_l\right] \left(\boldsymbol{\varepsilon}(\mathbf{u})^T : \mathbb{C} : \boldsymbol{\varepsilon}(\mathbf{u})\right) \, \mathrm{dV}, \tag{36}$$

then for all $\mathbf{x} \in \Omega$, $\mathfrak{d} \in [0, 1]$ implies that $\left[(1-\mathfrak{d})^2 + K_l\right] \geq 0$. Hence, the Eq. (36) can be bounded using Eq. (35) as

$$\Psi(\mathbf{u}, \mathfrak{d})\Big|_{E_B} \leq \Psi(\mathbf{u}, \mathfrak{d}) \leq \Psi(\mathbf{u}, \mathfrak{d})\Big|_{E_A}.$$

[1] [Note that Youngs modulus E is many orders of magnitude larger than Poisson ratio ν, and hence the effect of ν is almost zero].

Now, if $E_B > E_A$, then the above arguments holds true with $E_A \leq E(\mathbf{x}) \leq E_B$ and hence the inequality now takes the form

$$\Psi(\mathbf{u}, \mathfrak{d})\Big|_{E_A} \leq \Psi(\mathbf{u}, \mathfrak{d}) \leq \Psi(\mathbf{u}, \mathfrak{d})\Big|_{E_B}.$$

In both case, the elastic energy is bounded by its homogeneous constituent materials.

Part-2:- We will only prove for the case $E_A > E_B$, since the case $E_B > E_A$ is a trivial extension. Consider the surface energy of the FGM

$$\Psi_c(\mathfrak{d}) = \int_\Omega \frac{G_C(\mathbf{x})}{2l(\mathbf{x})}\mathfrak{d}^2 + G_C(\mathbf{x})l(\mathbf{x})\left|\nabla\mathfrak{d}\right|^2 \ \mathrm{dV},$$

From Eq. (7) , we have

$$G_C(\mathbf{x}) = \frac{\left(1-\nu(\mathbf{x})^2\right)K_{IC}^2(\mathbf{x})}{E(\mathbf{x})}, \qquad l(\mathbf{x}) = \frac{27}{256}\left(\frac{G_C(\mathbf{x})E(\mathbf{x})}{\sigma_c^2(\mathbf{x})}\right)$$

Surface energy can be bounded by the following chain of inequalities.

$$\begin{aligned}
&\int_\Omega \frac{256\sigma_{min}^2}{27E_A}\mathfrak{d}^2 + \frac{27\left(1-\nu(\mathbf{x})^2\right)^2 K_{IC}^4(\mathbf{x})}{256\sigma_{min}^2 E_A}\left|\nabla\mathfrak{d}\right|^2 \ \mathrm{dV} \\
\leq &\int_\Omega \frac{256\sigma_c^2(\mathbf{x})}{27E(\mathbf{x})}\mathfrak{d}^2 + \frac{27\left(1-\nu(\mathbf{x})^2\right)^2 K_{IC}^4(\mathbf{x})}{256\sigma_c^2(\mathbf{x})E(\mathbf{x})}\left|\nabla\mathfrak{d}\right|^2 \ \mathrm{dV} \\
\leq &\int_\Omega \frac{256\sigma_{max}^2}{27E_B}\mathfrak{d}^2 + \frac{27\left(1-\nu(\mathbf{x})^2\right)^2 K_{IC}^4(\mathbf{x})}{256\sigma_{max}^2 E_B}\left|\nabla\mathfrak{d}\right|^2 \ \mathrm{dV}
\end{aligned} \tag{37}$$

Case-1 When $\sigma_{min} = \sigma_A$ and $\sigma_{max} = \sigma_B$

If $\sigma_{min} = \sigma_A$ **and** $\sigma_{max} = \sigma_B$ meaning that $\sigma_B \geq \sigma_A$, then $\sigma(\mathbf{x}) \in [\sigma_A, \sigma_B]$, then the surface energy of FGM is trivially bounded between its homogeneous constituents. i.e

$$\Psi_c(\mathfrak{d})\Big|_A \leq \Psi_c(\mathfrak{d}) \leq \Psi_c(\mathfrak{d})\Big|_B.$$

Case-2: When $\sigma_{min} = \sigma_B$ and $\sigma_{max} = \sigma_A$.

If $\sigma_{min} = \sigma_B, \sigma_{max} = \sigma_A$ then the bound for surface energy in terms of its homogeneous constituents exist if

$$\frac{\sigma_{min}^2}{E_A} \leq \frac{\sigma^2(\mathbf{x})}{E(\mathbf{x})} \leq \frac{\sigma_{max}^2}{E_B}$$

is true.

In many materials, $E(\mathbf{x})$ is some orders of magnitude greater than $\sigma^2(\mathbf{x})$, (assuming that both are in MPa) otherwise, clearly $\sigma^2(\mathbf{x})$ is dominant. But in some materials, $E(\mathbf{x})$ can be of same order or less than $\sigma^2(\mathbf{x})$. Under these circumstances, we incorporate an extra condition such as the function $f(x) = \frac{\sigma^2(\mathbf{x})}{E(\mathbf{x})}$ is monotone. Thus, if $f(x)$ is monotonic, then clearly the extremes of the function lies on the boundaries since $f(x)$ is bounded function. Hence, we have

$$\frac{\sigma^2}{E}\Big|_A \leq \frac{\sigma^2(\mathbf{x})}{E(\mathbf{x})} \leq \frac{\sigma^2}{E}\Big|_B \quad or \quad \frac{\sigma^2}{E}\Big|_B \leq \frac{\sigma^2(\mathbf{x})}{E(\mathbf{x})} \leq \frac{\sigma^2}{E}\Big|_A,$$

depending on weather the function is monotonically increasing or decreasing. Hence substituting this in the surface energy inequality Eq. (37), we have that surface energy of FGM is bounded by its homogeneous

constituents if the function $f(\mathbf{x})$ is monotone[2] [3]. Physically, this also means that the function $f(\mathbf{x})$ is also constituent for the crack driving force and not just $E(\mathbf{x})$. □

5.3.1. Effect of grading on the Young's modulus

Consider a pre-cracked plate with displacement on one side of the boundary and fix the other side as shown in the Figure 5. In this specimen configuration, a denotes the length of the initial crack, b and w are the height and the width centered at $(0, 0)$. In this section, we consider values of $K_{1cA} = 3.5\text{MPa}\sqrt{\text{m}}$, $K_{1cB} = 8\text{MPa}\sqrt{\text{m}}$, $\nu_A = 0.21$ and $\nu_B = 0.31$ as the effects of small perturbation to their values shows to be non-sensitive and have no significant difference in the overall system behaviour. The model is discretized with 118400 4-node quadrilateral plane stress elements.

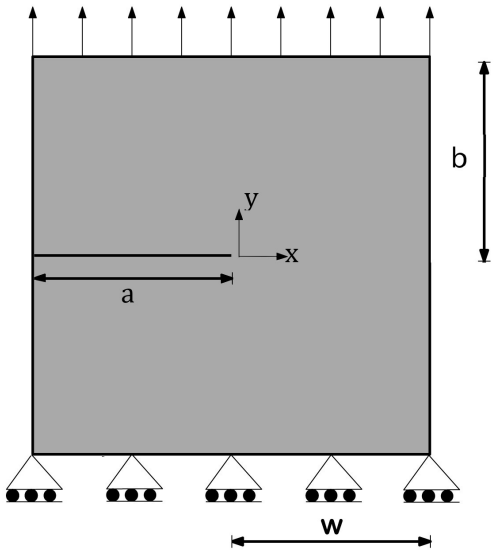

Figure 5: Plate with an edge crack under uni-axial tension.

In the context of crack propagation, the initial characterization for FGM can be done in terms of elastic mismatch and further can be made based on the apparent strength. Theoretically, it is possible to create a functionally graded materials with any combination of materials and hence it is better to consider an abstract value than that of the exact material properties so that the extreme effects can be simulated for further research development. To support this claim, consider Alumina-Zircona which has Young's modulus ratio of approximately 1.65, similarly Aluminum-Alumina, Alumina-Silica, Alumina-Epoxy have ratios of 4.78, 10, 100 respectively, see [9] for more details. Hence, in this section, we consider four ratios of $\frac{E_A}{E_B}$ with 2,5,10 and 20 by setting $E_A = 300$ GPa, to demonstrate the effects of elastic mismatch.

As in Theorem 3, the influence of Young's modulus cannot be considered in a separate manner, since the effect of fracture stress plays a major role in the crack propagation and surface energy release rates of the

[2] **Note:** The case that $f(\mathbf{x})$ is not monotone would arise if $\frac{\sigma^2_{min}}{E_A} \simeq \frac{\sigma^2_{max}}{E_B}$, in other words if the ratio $\left(\frac{\sigma_{min}}{\sigma_{max}}\right)^2 \left(\frac{E_{min}}{E_{max}}\right) \simeq 1$,then the bounds are very tight and hence the function $f(\mathbf{x})$ losses its monotonicty since $f(\mathbf{x})$ is quadratic function. Example of such case is given in Figure 9. Also notice that if the ratio $\left(\frac{\sigma_{min}}{\sigma_{max}}\right)^2 \left(\frac{E_{min}}{E_{max}}\right) < 1$, then the system behaves like in case-1 and hence bounds are guaranteed. We give numerical example showing all the cases in the example-1.

[3] **Note:** Notice that the constants in the non-local part of the surface energy is very small due to the product $\sigma^2(\mathbf{x})E(\mathbf{x})$, also the variation of the surface energy would lead to negative constants and hence have no effect on the bounds.

	E_A(GPa)	E_B(GPa)	σ_A(MPa)	σ_B(MPa)	$K_{IC,A}$ (MPa$\sqrt{\text{m}}$)	$K_{IC,B}$(MPa$\sqrt{\text{m}}$)	ν_A	ν_B
Case-1	300	150	600	300	3.5	8	0.21	0.31
Case-2			300	600				

Table 2: Material Properties for $\frac{E_A}{E_B} = 2$

FGM. For this reason, we consider cases when material A has strength greater than material B (Case-1 in Theorem 3) and when material B has greater strength than material-A (Case-2 in Theorem 3). The reaction curves for the $\frac{E_A}{E_B} = 2$ can be seen in Fig. 6 with material properties as reported in Table 2 along with their constitutive behaviour as in Eq. (33) and (34) for different values of the grading constant K. Similarly, for the reaction curves for the ratios $\frac{E_A}{E_B} = 5$ and $\frac{E_A}{E_B} = 10$ are given in Fig. 7.

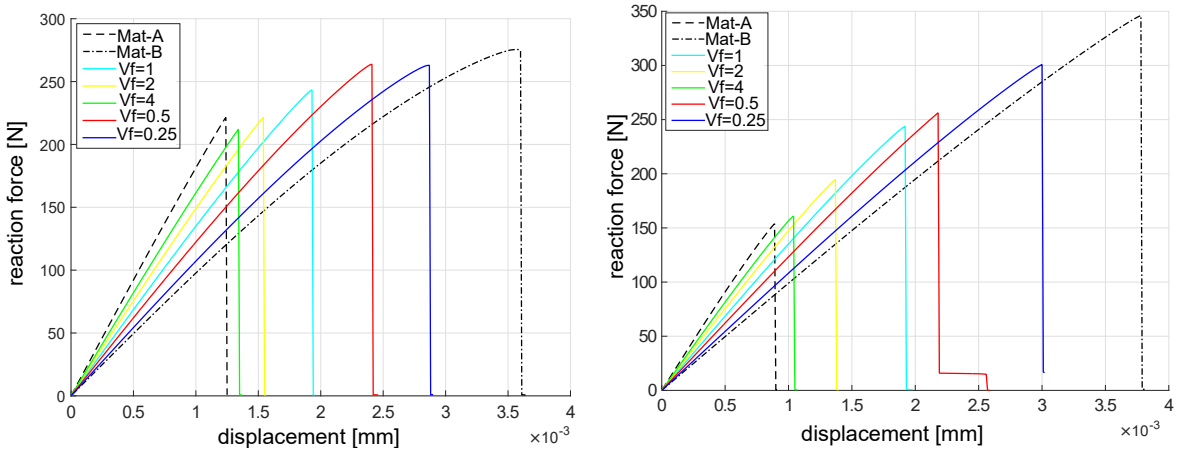

Figure 6: Material properties for $\frac{E_A}{E_B} = 2$ (Left) Reaction forces for the case-1, (Right) Reaction forces for case-2.

q

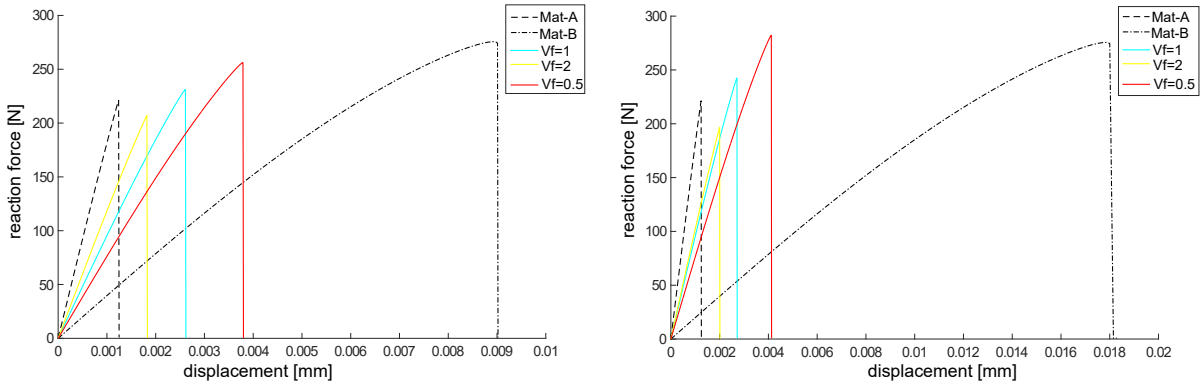

Figure 7: Reaction curves with $\sigma_A = 600$MPa and $\sigma_B = 300$ MPa for (Left) $\frac{E_A}{E_B} = 5$, (Right) $\frac{E_A}{E_B} = 10$

Analyzing the present results, it is possible to observe that when $\frac{E_A}{E_B} = 20$ is considered, as in Fig. 8, the results are not different from that outlined in Theorem 3. For any material property with $\frac{E_A}{E_B} = 20$ (which

is usually the case), the difference in length scale parameter is at least one order magnitude greater than the smallest length scale. In such cases, relying on the present computational results, we can argue that the variation of the length scale within the specimen domain cannot be neglected. We have also shown previously that the failure stress plays a major role in the crack propagation which is inversely proportional to the length scales, which is also consistent with the previous investigations on the matter, see [34, 86, 61, 66].

Continuing with the analysis of the present results, we notice that with the material properties used to obtain the results plotted in Fig. 6, 7 and 8, the crack propagation direction is towards minimum Young's modulus. The steepness in the reaction forces representing the crack nucleation is due to the mismatch in Young's modulus. As expected, configurations with the highest mismatch exhibit the steepest gradients. The FGM variation in this case is linear as the difference in mechanical energy release rate due to the change of grading of volume fraction is linear, see Eq. (35). This implies, depending on the volume fraction, the crack nucleation in the FGM is a linear combination of its homogeneous constituents. Similarly, σ determines the maximum value (cut-off) of the reaction curves, with a trend consistent with what is expected for homogeneous materials. FGM formed due to variation of σ in turn on l is quadratic in nature from Eq. (7). Meaning that, depending on volume fraction and $\frac{\sigma^2}{E}$ ratio, the apparent strength is a quadratic combination of its homogeneous constituents. In order to understand what happens when the monotonicity of $\frac{\sigma^2}{E}$ is lost, consider the following example with the Young's modulus ratio $\frac{E_A}{E_B} = 1.5$, and $\sigma_A = 300$ MPa and $\sigma_B = 245$ MPa and keeping the rest as in Table-2 can be seen in Fig. 9. Even though all intrinsic material properties are monotone, the ratio of $\frac{\sigma^2}{E}$ is not monotonic so far, and hence the surface energies neither fall under case-1 nor case-2, hence crack propagation and the reaction forces of these FGMs cannot be predicted using its homogeneous constituents only in an accurate manner. This aspect suggests that the crack path cannot be easily predicted, requiring either the conduction of a careful experimental campaign (producing such complex samples) or the use of suitable numerical models that enabling capturing such intricate response.

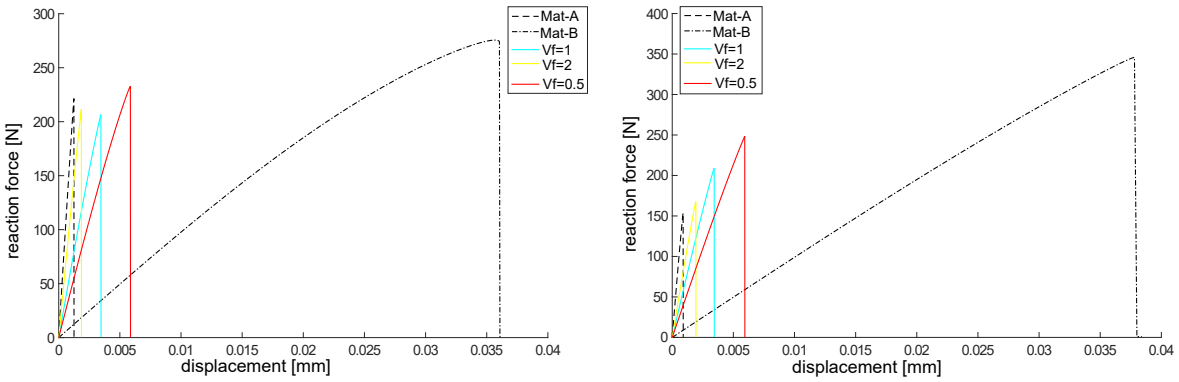

Figure 8: (Left) Reaction forces for the case-1, (Right) Reaction forces for case-2 with $\frac{E_A}{E_B} = 20$.

5.3.2. Effect of initial crack position and crack length

In this subsection, we explore the effect of the initial crack position and crack length in the FGM with linear grading, by considering $\frac{E_A}{E_B} = 2$, with $E_A = 300$ GPa and $\sigma_A = 600$MPa and $\sigma_B = 300$MPa, $K_{1cA} = 3.5$ MPa$\sqrt{\text{m}}$ and $K_{1cA} = 8$ MPa$\sqrt{\text{m}}$. The overall behavior with respect to any other cases (as well as grading profiles) are similar. In this concern, if a represents the length of crack as in Fig. 5, keeping the $w = b = 10$ the variation of the crack length keeping everything else the same results in the reaction curves as shown in Fig. 10 (a). Stemming from these results, it becomes evident that, as the initial crack length decreases the elastic energy required for the crack to propagate is higher. Hence, we can see that

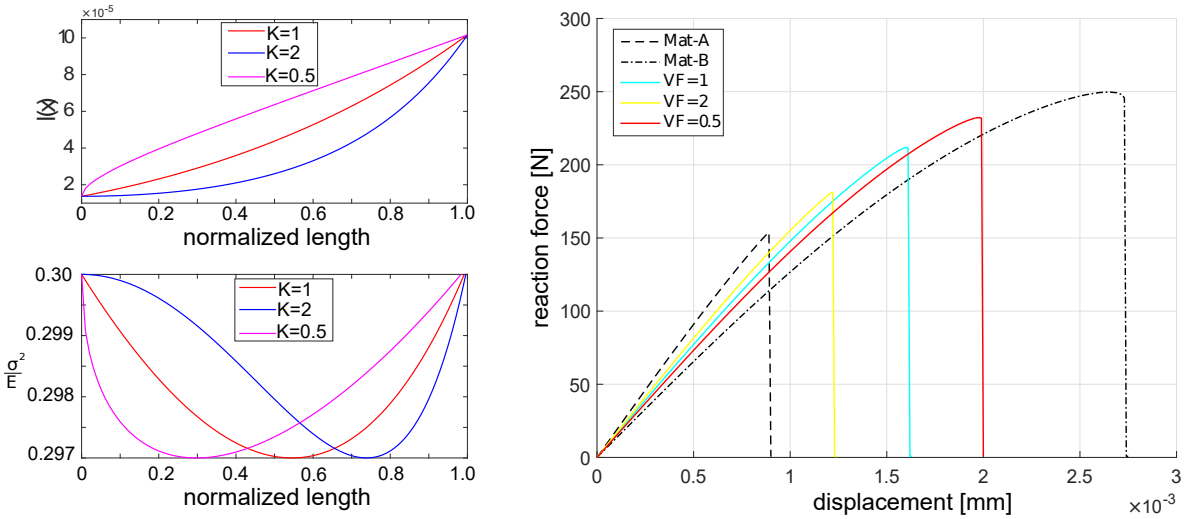

Figure 9: Material properties along with $\frac{E_A}{E_B} = 1.5$ (Left) Material Properties, (Right) Corresponding Reaction forces.

the steepness in reaction curves due to the elastic energy release rate increases as crack length decreases. Similarly, the surface energy required for the material to fracture is also higher with decrease in crack length.

In line with the previous discussion, if a square plate with $a = w = b = 10$ in Fig. 5 is taken, but the crack is placed at a distance c in the y-direction from center of the specimen, then we obtain the results depicted in Fig. 10 (b). Analyzing this graph, we can observe that the overall mechanical energy is nearly coincident for all the experiments, since the initial crack length is the same for each of the cases, but the surface energy is slightly different from each other due to asymmetric loading on the crack tip. As a major conclusion, by changing position of the initial crack tip in the direction of increasing $\frac{\sigma^2}{E}$ would decrease the surface energy.

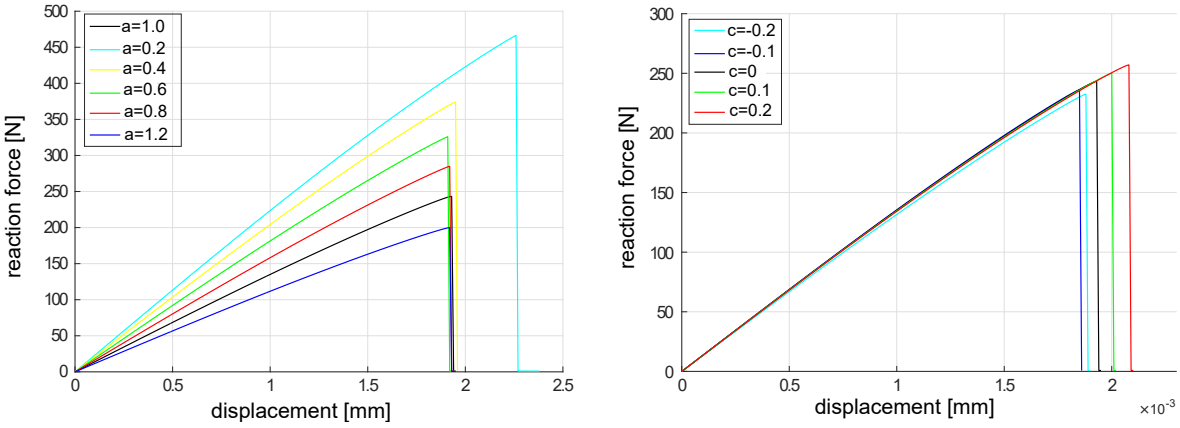

Figure 10: Load-displacement curves for (Left) change of crack length (Right) change of crack position.

Figure 11 shows the reaction curves for different grading profiles. From this graph, it is easy to notice that, if the grading direction is along the x-axis (Grading-6 as in 11) opposite to the crack propagation path, the reaction curves shows a gradual drop. Also, Grading-1, Grading-2 , Grading-3 and Grading-4 profiles has

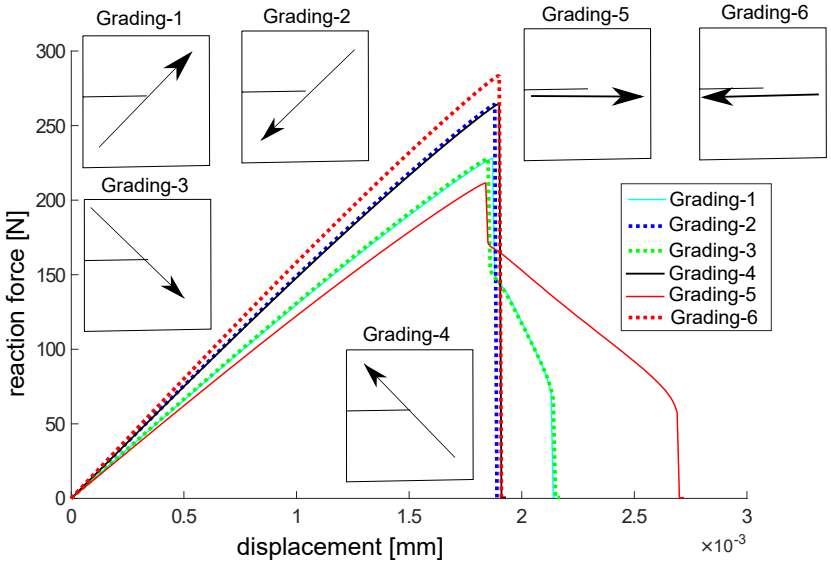

Figure 11: Load-displacement curves for different grading profiles

different material properties at their crack tip and the corresponding reaction curves shows similar surface energies release rates but different elastic energy release rate.

5.3.3. Size-scale effects

In this subsection, we consider the size-scale effects for FGMs with linear grading and keeping the material properties as in Subsection 5.3.2, while change the dimensions w to account for a square specimen. If we scale the Fig. 5 including also the crack length, keeping the internal length scale constant, it is easy to see from Eq.(8) that the potential energy increases as the domain is expanded. Also, from the numerical viewpoint, the same conclusion holds for the reaction forces, whilst the elastic energy release rate is kept constant but the surface energy release becomes higher. Since the maximum reaction force is directly proportional to the maximum surface energy release rate, it is also interesting to see that the scaling factor follows a power law as in Fig. 12(b). This constitutes the main idea of the $\Gamma-$convergence proof presented in Section 3.

We emphasize on the equivalence relation that, from Eq. (13) and Eq. (17) it is easy to see that for every increase in size (of domain) of Eq. (13), there exists a ϵ in Eq. (17) such that the bulk and the surface energies are equal due to continuous mapping S_u. Meaning that, it is possible to find a ϵ value in Eq. (17) which mimics the size-scale effects of Eq. (13). This idea can have direct applications in engineering design and analysis.

Recalling this idea, let consider a problem of fracture on a large model, which is possible to reduce to model to a very small convenient size and find the ϵ such that the reduced model mimics the original one. For example, by setting $b = w = 10$, ϵ value for Eq. (17) using the following straightforward relation $b' = \frac{1}{2}(1+\frac{1}{\epsilon})b$, to mimic any value of b'. For $b' = 25, 50, 100$, the value of $\epsilon = 0.25, 0.110, 0.05263$ respectively are equivalent. Meaning that, it is possible to simulate the behaviour of the model $b' = 25$, with $\epsilon = 0.25$ and $b = 10$ from Eq. (17). As one expects, the comparison between numerical experiments done using Eq. (13) and Eq. (17) would give same results as in Fig. 12(b). For $b \neq w$, ϵ is calculated by the approximate area of the domain such that $b'w' = (\frac{1}{2}(1 + \frac{1}{\epsilon}))^2 bw$ for some fixed b, w.

Also, it can be seen from the power law that as the scaling approaches infinity in Eq. (13) (or ϵ approaches zero from Eq. (17)), the maximum reaction force also approach infinity asymptotically, hence can be considered as the numerical evidence for $\Gamma-$Convergence.

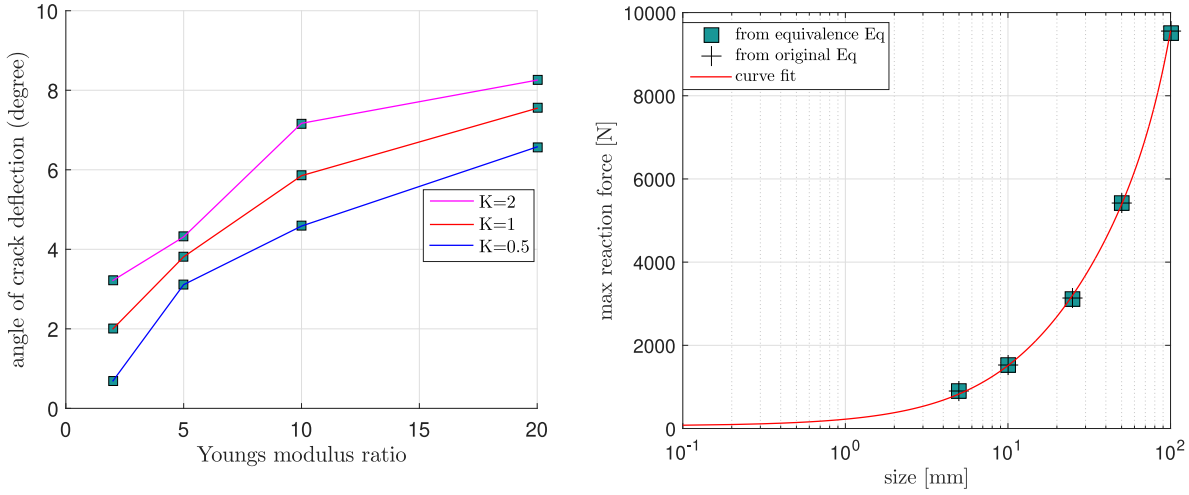

Figure 12: (Left) angle of crack deflection due to different Young's modulus ratio (Right) maximum reaction due to size effects.

5.4. Micromechanical application

In this subsection, the proposed model is applied to a fiber-reinforced specimen with a functionally graded material matrix. This application intends to revisiting the cases presented in [39, 51] for homogeneous matrix. Nevertheless, differing from precedent investigations of the authors [39], we neglect the potential presence of fibre-matrix decohesion events (usually modelled via interface-like models) in order to preserve the main focus of the current investigation. In addition to the previous considerations, it is worth mentioning that the present application inherently incorporates different scale separations due to he homogenized FGM properties in the matrix (which implies a FGM microstructure) and the explicit discretization of the fiber. A more careful analysis scale separation assumptions could be investigated via the methodology developed in [87].

The baseline single-fiber domain is subjected to transverse loading conditions from micro-mechanical perspective is considered as in [39] and the reference therein. A squared 2D domain complying with a brittle response contains a circular fibre, see Fig. 13. The domain is meshed with 120000 first order plane-stress elements and 1000 steps are used to run the computations under displacement control.

The system properties consists of circular transverse section of side length vs radius $\frac{L}{R} = 4$. Both, the fiber and the matrix are considered to obey a linear elastic material behaviour with a FGM matrix. Without any loss of generality, the baseline properties for the present numerical investigations recall some standard values previously reported in the related literature [39]. In this regard, the properties of the fiber is taken to be $E_f = 78$ GPa and Poisson's ratio of $\nu_f = 0.22$. The FGM properties are $E_A = 2.8$ GPa, $\nu_A = 0.33$, $G_{C,A} = 0.016\ \frac{N}{mm}$. Keeping these properties constant, the material properties such as E_B, $G_{C,B}$ are varied to understand the effects of different grading, and preserving the ratio $\frac{E_f}{E_A} = 27.8$ throughout the section in conjunction with varying $\frac{E_A}{E_B}$ ratio and $\frac{G_{C,A}}{G_{C,B}}$ ratio.

The dimensionless parameters $\frac{d}{L}$ for the applied displacement d is plotted against $\frac{R}{L\sigma_A}$ (R denoting R is overall reaction forces at left edge of the system) for different Young's Modulus ratio $\frac{E_A}{E_B}$ with $\frac{G_{C,A}}{G_{C,B}} = 2$, see Fig. 14.a. Similarly, the variation of fracture toughness ratio $\frac{G_{C,A}}{G_{C,B}}$, keeping $\frac{E_A}{E_B} = 2$ constant is plotted in Fig. 14.b for the comprehensive visualization of the spatial variability regarding the material properties. Analyzing these results, it is observed that, as the Young's modulus ratio increases, the asymmetry in the loading increases leading to asymmetrical crack propagation. Fig. 15 depicts the crack initiation and propagation condition for the different ratio of Young's modulus. As mentioned earlier as in Theorem-3.

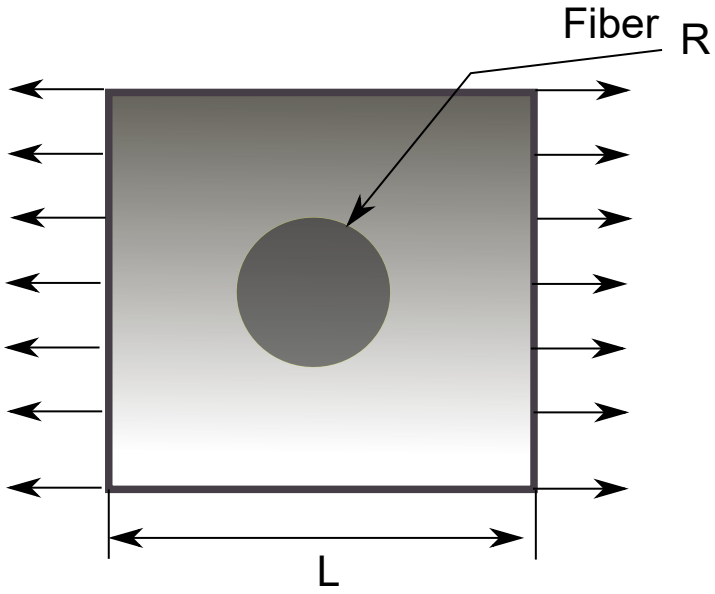

Figure 13: Micromechanics of fiber-reinforced FGM material under transverse tensile loading conditions: geometry and boundary conditions.

The asymmetry is the case of single-fiber transverse loading starts towards the lowest Young's modulus side.

For $\frac{E_A}{E_B} = 2$, crack propagation happens from only one side and, in subsequent loading stages, a secondary crack starts appearing on the other side of the fibre-matrix edge, see Fig. 15. This behaviour is also reflected in the reaction force curve which displays two sudden drops, see Fig. 14a. For $\frac{E_A}{E_B} \geq 5$, crack propagation is asymmetrical, see Fig. 15. The $\frac{G_{C,A}}{G_{C,B}}$ ratio plays a significant role in crack propagation, as the $\frac{G_{C,A}}{G_{C,B}}$ ratio increases, the reaction force also increases and delays the crack nucleation. Finally, with respect to the cracking pattern for different $\frac{E_A}{E_B}$ values (Fig. 16), we observe a general trend in this numerical experiment exhibiting a lower kinking angle towards the matrix of the main crack as $\frac{E_A}{E_B}$ decreases.

6. Conclusions

In this article, the phase field approximation of fracture in FGM's by considering variation of material properties has been proposed by considering the internal length scale of the phase field as a characteristic property of the material. The proof of Γ-Convergence has been provided when the characteristics internal length scale l is constant or is a bounded function. It can be seen from the power law that as the scaling approaches infinity in Eq. (13) (or ϵ approaches zero from Eq. (17)), the maximum reaction force also approach infinity asymptotically, hence can be considered as the numerical evidence for $\Gamma-$Convergence.

As an engineering application, it is possible to exploit the theoretical results upon size-scale effects to design experiments on scaled down specimens which do reproduce the behaviour of the real (full-scale) ones, by varying material properties. Moreover, it is shown that $\frac{\sigma^2}{E}$, and position of the initial crack tip affects the crack propagation and not only $E(\mathbf{x})$.

Acknowledgements

JR is grateful to the Consejería de Economía y Conocimiento of the Junta de Andalucía (Spain) for financial support under the contract US-1265577-Programa Operativo FEDER Andalucía 2014-2020.

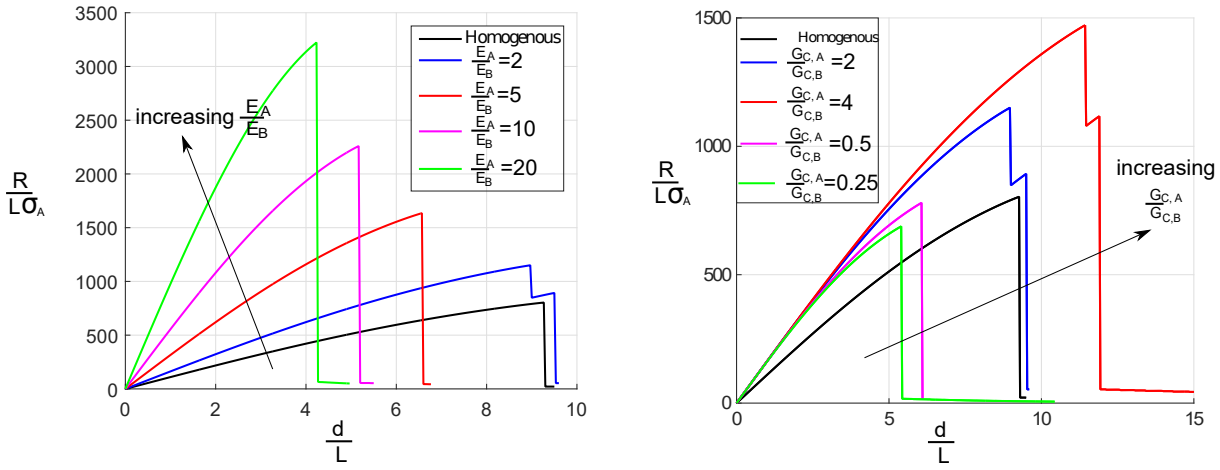

Figure 14: $\frac{R}{L\sigma_A}$ vs $\frac{L}{d}$ ratio for different (left) Young's modulus ratio (right) fracture toughness ratio.

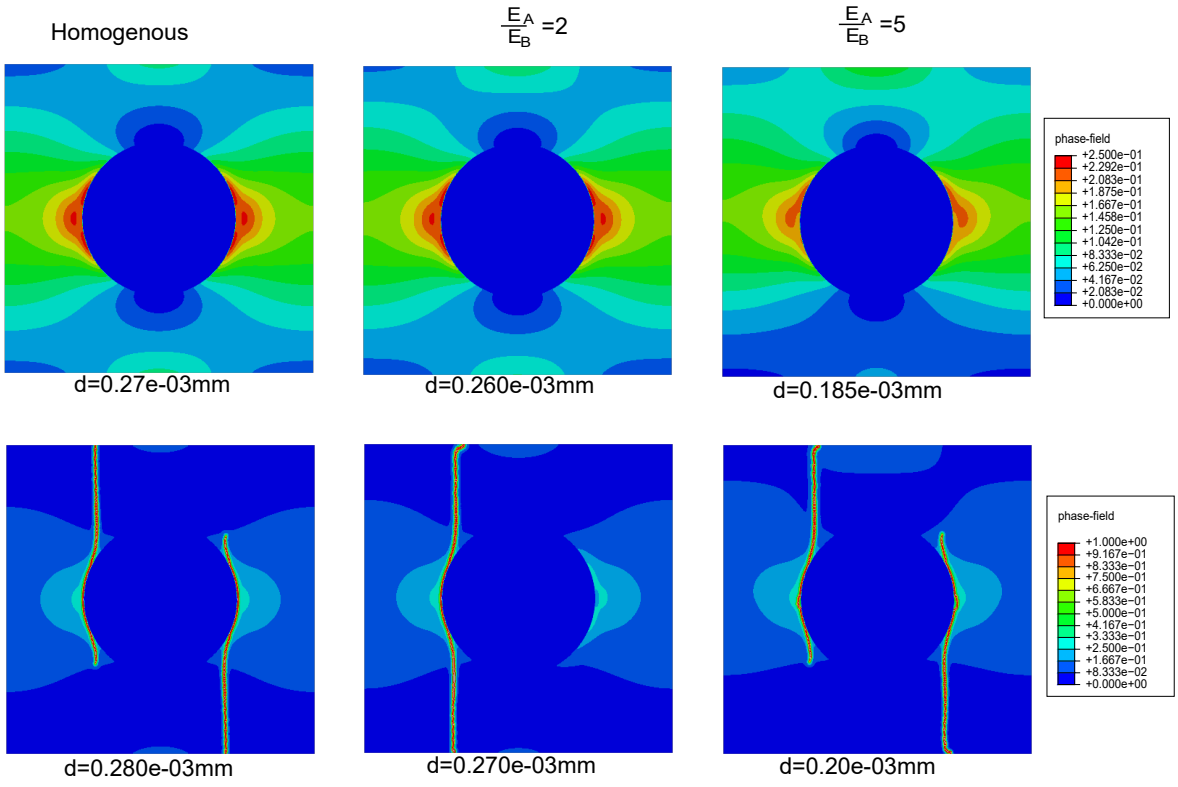

Figure 15: Crack initiation and crack propagation in single fiber reinforced composite due to different material conditions.

JR acknowledges Prof. Dominique Leguillon (CNRS - Sorbonne Université) for inspiring and fruitful discussions on this matter.

MP would like to acknowledge the financial support of the Italian Ministry of Education, University and

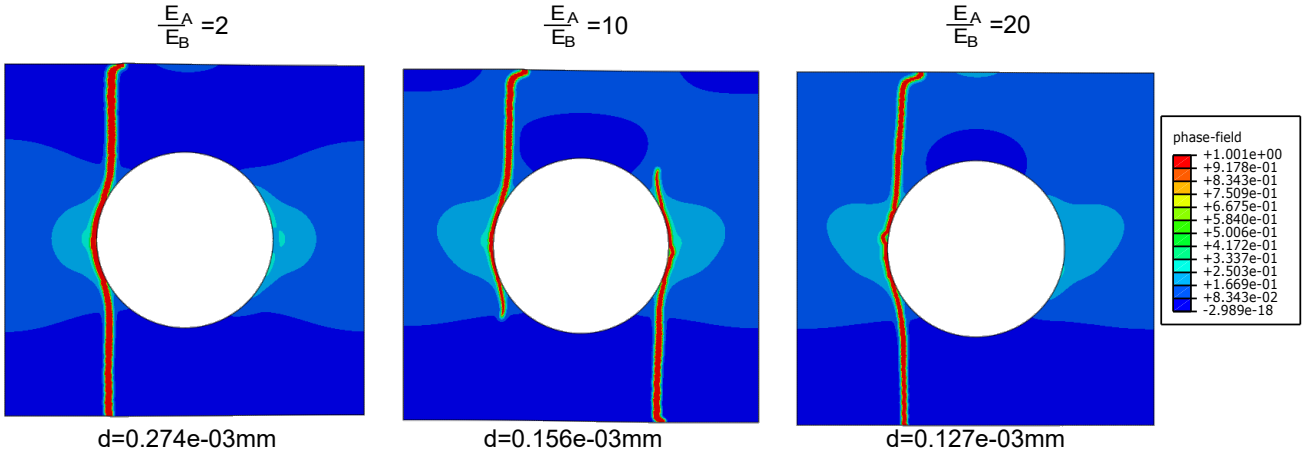

Figure 16: Crack propagation in single fiber reinforced composite.

Research to the Research Project of National Interest (PRIN 2017) XFAST-SIMS "Extra fast and accurate simulation of complex structural systems", CUP: D68D19001260001.

References

[1] Niino.M, Hirai.T, Watanabe.R, The functionally gradient materials, Jap Soc Compos Mat 13: 257-64. (1987).
[2] N. Rödel.J, Gradient materials: An overview of a novel concept, Zeit Metall 88: 358-71. (1997).
[3] H. Bahr, H. Balke, T. Fett, I. Hofinger, G. Kirchhoff, D. Munz, A. Neubrand, A. Semenov, H. Weiss, Y. Yang, Cracks in functionally graded materials, Materials Science and Engineering: A 362 (1) (2003) 2–16, papers from the German Priority Programme (Functionally Graded Materials). doi:10.1016/S0921-5093(03)00582-3.
[4] A. Moro, Y. Kuroda, K. Kusaka, Development status of the reusable high-performance engines with functionally graded materials, Acta Astronautica 50 (2002) 427–432. doi:10.1016/S0094-5765(01)00174-6.
[5] C. Chu, J. Zhu, Z. Yin, P. Lin, Structure optimization and properties of hydroxyapatite-ti symmetrical functionally graded biomaterial, Materials Science and Engineering: A 316 (1) (2001) 205 – 210. doi:https://doi.org/10.1016/S0921-5093(01)01239-4.
[6] T. Guillén-Hernández, J. Reinoso, M. Paggi, Phase field model for fracture analysis of functionally graded power-based shell structures, Mechanics of Advanced Materials and Structures 0 (0) (2020) 1–11. doi:10.1080/15376494.2020.1751354.
[7] F. Delale, F. Erdogan, The Crack Problem for a Nonhomogeneous Plane, Journal of Applied Mechanics 50 (3) (1983) 609–614. doi:10.1115/1.3167098.
[8] N. Konda, F. Erdogan, The mixed mode crack problem in a nonhomogeneous elastic medium, Engineering Fracture Mechanics 47 (4) (1994) 533 – 545. doi:https://doi.org/10.1016/0013-7944(94)90253-4.
[9] M. T. Tilbrook, Fatigue crack propagation in functionally graded materials, Ph.D. thesis, School of Materials Science & Engineering, University of New South Wales (2005).
[10] F. Erdogan, Fracture mechanics of functionally graded materials, Composites Engineering 5 (7) (1995) 753 – 770. doi:https://doi.org/10.1016/0961-9526(95)00029-M.
[11] Z.-H. Jin, R. Batra, Some basic fracture mechanics concepts in functionally graded materials, Journal of the Mechanics and Physics of Solids 44 (8) (1996) 1221 – 1235. doi:https://doi.org/10.1016/0022-5096(96)00041-5.
[12] P. Gu, R. Asaro, Cracks in functionally graded materials, International Journal of Solids and Structures 34 (1) (1997) 1 – 17. doi:https://doi.org/10.1016/0020-7683(95)00289-8.
[13] P. Gu, R. Asaro, Crack deflection in functionally graded materials, International Journal of Solids and Structures 34 (24) (1997) 3085 – 3098. doi:https://doi.org/10.1016/S0020-7683(96)00175-8.
[14] J. Dolbow, J. Nadeau, On the use of effective properties for the fracture analysis of microstructured materials, Engineering Fracture Mechanics 69 (14) (2002) 1607 – 1634. doi:https://doi.org/10.1016/S0013-7944(02)00052-8.
[15] J.-H. Kim, G. H. Paulino, Simulation of crack propagation in functionally graded materials under mixed-mode and non-proportional loading, Mechanics and Materials in Design 1 (1) (2004) 63–94. doi:10.1023/B:MAMD.0000035457.78797.c5.
[16] M. T. Tilbrook, R. J. Moon, M. Hoffman, Crack propagation in graded composites, Composites Science and Technology 65 (2) (2005) 201 – 220. doi:https://doi.org/10.1016/j.compscitech.2004.07.004.
[17] E. Martínez-Pañeda, On the finite element implementation of functionally graded materials., Materials (Basel, Switzerland) 12(2) (2019) 287. doi:10.3390/ma12020287.
[18] J. Reinoso, M. Paggi, R. Rolfes, A computational framework for the interplay between delamination and wrinkling in functionally graded thermal barrier coatings, Computational Materials Science 116 (2016) 82 – 95, articles from EUROMECH

Colloquium 577 “Micromechanics of Metal Ceramic Composites”. doi:https://doi.org/10.1016/j.commatsci.2015.08.031.
URL http://www.sciencedirect.com/science/article/pii/S0927025615005406
[19] M. Steigemann, M. Specovius-Neugebauer, M. Fulland, H. Richard, Simulation of crack paths in functionally graded materials, Engineering Fracture Mechanics 77 (11) (2010) 2145 – 2157. doi:https://doi.org/10.1016/j.engfracmech.2010.03.022.
[20] J. W. Eischen, Fracture of nonhomogeneous materials, International Journal of Fracture 34 (1) (1987) 3–22. doi:10.1007/BF00042121.
[21] P. Gu, M. Dao, R. J. Asaro, A Simplified Method for Calculating the Crack-Tip Field of Functionally Graded Materials Using the Domain Integral, Journal of Applied Mechanics 66 (1) (1999) 101–108. doi:10.1115/1.2789135.
[22] G. Anlas, M. Santare, J. Lambros, Numerical calculation of stress intensity factors in functionally graded materials, International Journal of Fracture 104 (2) (2000) 131–143. doi:10.1023/A:1007652711735.
[23] G. Bao, L. Wang, Multiple cracking in functionally graded ceramic/metal coatings, International Journal of Solids and Structures 32 (19) (1995) 2853 – 2871. doi:https://doi.org/10.1016/0020-7683(94)00267-Z.
[24] J.-H. Kim, G. H. Paulino, Finite element evaluation of mixed mode stress intensity factors in functionally graded materials, International Journal for Numerical Methods in Engineering 53 (8) (2002) 1903–1935. doi:10.1002/nme.364.
[25] C. Comi, S. Mariani, Extended finite element simulation of quasi-brittle fracture in functionally graded materials, Computer Methods in Applied Mechanics and Engineering 196 (41) (2007) 4013 – 4026. doi:https://doi.org/10.1016/j.cma.2007.02.014.
URL http://www.sciencedirect.com/science/article/pii/S0045782507001697
[26] H. Bayesteh, S. Mohammadi, Xfem fracture analysis of orthotropic functionally graded materials, Composites Part B: Engineering 44 (1) (2013) 8 – 25. doi:https://doi.org/10.1016/j.compositesb.2012.07.055.
URL http://www.sciencedirect.com/science/article/pii/S1359836812005100
[27] Martínez-Pañeda, E. Gallego, Numerical analysis of quasi-static fracture in functionally graded materials, Int J Mech Mater Des 11 (2015) 405–424. doi:https://doi.org/10.1007/s10999-014-9265-y.
URL https://link.springer.com/article/10.1007/s10999-014-9265-yciteas
[28] N. S. S. Ooi, E.T., Crack propagation modelling in functionally graded materials using scaled boundary polygons, International journal of fracture 192 (2015) 87–105. doi:https://doi.org/10.1007/s10704-015-9987-3.
[29] Z.-H. Jin, G. Paulino, R. Dodds Jr., Finite element investigation of quasi-static crack growth functionally graded materials using a novel cohesive zone fracture model, Journal of Applied Mechanics, Transactions ASME 69 (3) (2002) 370–379. doi:10.1115/1.1467092.
[30] S. Kandula, J. Abanto-Bueno, P. Geubelle, J. Lambros, Cohesive modeling of dynamic fracture in functionally graded materials, Int J Fract 132 (3) (2005) 275–296.
[31] C. Li, Z. Zou, Z. Duan, Multiple isoparametric finite element method for nonhomogeneous media, Mechanics Research Communications 27 (2) (2000) 137 – 142. doi:https://doi.org/10.1016/S0093-6413(00)00073-2.
[32] J.-H. Kim, G. Paulino, Isoparametric graded finite elements for nonhomogeneous isotropic and orthotropic materials, Journal of Applied Mechanics, Transactions ASME 69 (4) (2002) 502–514. doi:10.1115/1.1467094.
[33] Z. J. Zhang, G. H. Paulino, Cohesive zone modeling of dynamic failure in homogeneous and functionally graded materials, International Journal of Plasticity 21 (6) (2005) 1195 – 1254, plasticity of Multiphase Materials. doi:https://doi.org/10.1016/j.ijplas.2004.06.009.
[34] Hirshikesh, S. Natarajan, R. K. Annabattula, E. Martínez-Pañeda, Phase field modelling of crack propagation in functionally graded materials, Composites Part B: Engineering 169 (2019) 239 – 248. doi:https://doi.org/10.1016/j.compositesb.2019.04.003.
[35] H. Saberi, T. Q. Bui, A. Furukawa, A. Rahai, S. Hirose, Frp-confined concrete model based on damage-plasticity and phase-field approaches, Composite Structures 244 (2020) 112263. doi:https://doi.org/10.1016/j.compstruct.2020.112263.
[36] T.-T. Nguyen, D. Waldmann, T. Q. Bui, Role of interfacial transition zone in phase field modeling of fracture in layered heterogeneous structures, Journal of Computational Physics 386 (2019) 585 – 610. doi:https://doi.org/10.1016/j.jcp.2019.02.022.
[37] T.-T. Nguyen, D. Waldmann, T. Q. Bui, Computational chemo-thermo-mechanical coupling phase-field model for complex fracture induced by early-age shrinkage and hydration heat in cement-based materials, Computer Methods in Applied Mechanics and Engineering 348 (2019) 1 – 28. doi:https://doi.org/10.1016/j.cma.2019.01.012.
[38] P. Zhang, Y. Feng, T. Q. Bui, X. Hu, W. Yao, Modelling distinct failure mechanisms in composite materials by a combined phase field method, Composite Structures 232 (2020) 111551. doi:https://doi.org/10.1016/j.compstruct.2019.111551.
[39] T. Guillén-Hernández, I. G. García, J. Reinoso, M. Paggi, A micromechanical analysis of inter-fiber failure in long reinforced composites based on the phase field approach of fracture combined with the cohesive zone model, International Journal of Fracture (2019). doi:10.1007/s10704-019-00384-8.
URL https://doi.org/10.1007/s10704-019-00384-8
[40] A. Quintanas-Corominas, J. Reinoso, E. Casoni, A. Turon, J. Mayugo, A phase field approach to simulate intralaminar and translaminar fracture in long fiber composite materials, Composite Structures (2019). doi:10.1016/j.compstruct.2019.02.007.
[41] J. Reinoso, A. Arteiro, M. Paggi, P. Camanho, Strength prediction of notched thin ply laminates using finite fracture mechanics and the phase field approach, Composites Science and Technology 150 (2017) 205 – 216.
[42] V. Carollo, J. Reinoso, M. Paggi, A 3d finite strain model for intralayer and interlayer crack simulation coupling the phase field approach and cohesive zone model, Composite Structures 182 (2017) 636 – 651.
[43] E. Martínez-Pañeda, A. Golahmar, C. F. Niordson, A phase field formulation for hydrogen assisted cracking, Computer Methods in Applied Mechanics and Engineering 342 (2018) 742 – 761. doi:https://doi.org/10.1016/j.cma.2018.07.021.
URL http://www.sciencedirect.com/science/article/pii/S0045782518303529

[44] M. Dittmann, F. Aldakheel, J. Schulte, P. Wriggers, C. Hesch, Variational phase-field formulation of non-linear ductile fracture, Computer Methods in Applied Mechanics and Engineering 342 (2018) 71 – 94. doi:https://doi.org/10.1016/j.cma.2018.07.029.
URL http://www.sciencedirect.com/science/article/pii/S0045782518303621
[45] T. Guillén-Hernández, A. Quintana-Corominas, I. García, J. Reinoso, M. Paggi, A. Turón, In-situ strength effects in long fibre reinforced composites: A micro-mechanical analysis using the phase field approach of fracture, Theoretical and Applied Fracture Mechanics 108 (2020) 102621. doi:https://doi.org/10.1016/j.tafmec.2020.102621.
URL http://www.sciencedirect.com/science/article/pii/S016784422030197X
[46] O. Gültekin, H. Dal, G. A. Holzapfel, Numerical aspects of anisotropic failure in soft biological tissues favor energy-based criteria: A rate-dependent anisotropic crack phase-field model, Computer Methods in Applied Mechanics and Engineering 331 (2018) 23 – 52. doi:https://doi.org/10.1016/j.cma.2017.11.008.
URL http://www.sciencedirect.com/science/article/pii/S0045782517307132
[47] D. H. Doan, T. Q. Bui, N. D. Duc, K. Fushinobu, Hybrid phase field simulation of dynamic crack propagation in functionally graded glass-filled epoxy, Composites Part B: Engineering 99 (2016) 266 – 276. doi:https://doi.org/10.1016/j.compositesb.2016.06.016.
[48] D. H. Doan, T. Q. Bui, T. Van Do, N. D. Duc, A rate-dependent hybrid phase field model for dynamic crack propagation, Journal of Applied Physics 122 (11) (2017) 115102. doi:10.1063/1.4990073.
[49] T. Q. Bui, N. T. Nguyen, L. V. Lich, M. N. Nguyen, T. T. Truong, Analysis of transient dynamic fracture parameters of cracked functionally graded composites by improved meshfree methods, Theoretical and Applied Fracture Mechanics 96 (2018) 642 – 657. doi:https://doi.org/10.1016/j.tafmec.2017.10.005.
[50] A. Chambolle, An approximation result for special functions with bounded deformation, Journal de Mathématiques Pures et Appliquées 83 (7) (2004) 929 – 954. doi:https://doi.org/10.1016/j.matpur.2004.02.004.
URL http://www.sciencedirect.com/science/article/pii/S0021782404000285
[51] B. Bourdin, G. Francfort, J.-J. Marigo, Numerical experiments in revisited brittle fracture, Journal of the Mechanics and Physics of Solids 48 (4) (2000) 797 – 826. doi:https://doi.org/10.1016/S0022-5096(99)00028-9.
[52] L. Ambrosio, A. Braides, Energies in sbv and variational models in fracture mechanics. (1997).
[53] M. Negri, M. Paolini, Numerical minimization¶of the mumford–shah functional, CALCOLO 38 (2) (2001) 67–84. doi:10.1007/s100920170004.
[54] G. Francfort, J.-J. Marigo, Revisiting brittle fracture as an energy minimization problem, Journal of the Mechanics and Physics of Solids 46 (8) (1998) 1319 – 1342. doi:https://doi.org/10.1016/S0022-5096(98)00034-9.
[55] C. Chambolle, A., A density result in gsbdp with applications to the approximation of brittle fracture energies., Arch Rational Mech Anal 232, (2019) 1329–1378doi:https://doi.org/10.1007/s00205-018-01344-7.
[56] L. Ambrosio, A. Coscia, G. D. Maso, Fine properties of functions with bounded deformation, Arch. Rational Mech. Anal. 139 (1997) 201–238.
[57] C. Miehe, M. Hofacker, F. Welschinger, A phase field model for rate-independent crack propagation: Robust algorithmic implementation based on operator splits, Computer Methods in Applied Mechanics and Engineering 199 (45) (2010) 2765 – 2778. doi:https://doi.org/10.1016/j.cma.2010.04.011.
[58] C. Kuhn, A. Schlüter, R. Müller, On degradation functions in phase field fracture models, Computational Materials Science 108 (2015) 374 – 384, selected Articles from Phase-field Method 2014 International Seminar. doi:https://doi.org/10.1016/j.commatsci.2015.05.034.
[59] C. Kuhn, R. Müller, A continuum phase field model for fracture, Engineering Fracture Mechanics 77 (18) (2010) 3625 – 3634. doi:https://doi.org/10.1016/j.engfracmech.2010.08.009.
[60] A. Mesgarnejad, B. Bourdin, M. Khonsari, Validation simulations for the variational approach to fracture, Computer Methods in Applied Mechanics and Engineering 290 (2015) 420 – 437. doi:https://doi.org/10.1016/j.cma.2014.10.052.
[61] J. Abanto-Bueno, J. Lambros, An experimental study of mixed mode crack initiation and growth in functionally graded materials, Experimental Mechanics 46 (2) (2006) 179–196. doi:10.1007/s11340-006-6416-6.
[62] M. Tilbrook, K. Rozenburg, E. Steffler, L. Rutgers, M. Hoffman, Crack propagation paths in layered, graded composites, Composites Part B: Engineering 37 (6) (2006) 490 – 498. doi:https://doi.org/10.1016/j.compositesb.2006.02.012.
[63] H. Amor, J.-J. Marigo, C. Maurini, Regularized formulation of the variational brittle fracture with unilateral contact: Numerical experiments, Journal of the Mechanics and Physics of Solids 57 (8) (2009) 1209 – 1229. doi:https://doi.org/10.1016/j.jmps.2009.04.011.
[64] T. Nguyen, J. Yvonnet, Q.-Z. Zhu, M. Bornert, C. Chateau, A phase-field method for computational modeling of interfacial damage interacting with crack propagation in realistic microstructures obtained by microtomography, Computer Methods in Applied Mechanics and Engineering 312 (2016) 567 – 595, phase Field Approaches to Fracture. doi:https://doi.org/10.1016/j.cma.2015.10.007.
[65] E. Tanné, T. Li, B. Bourdin, J.-J. Marigo, C. Maurini, Crack nucleation in variational phase-field models of brittle fracture, Journal of the Mechanics and Physics of Solids 110 (2018) 80 – 99. doi:https://doi.org/10.1016/j.jmps.2017.09.006.
[66] M. Paggi, J. Reinoso, Revisiting the problem of a crack impinging on an interface:a modeling framework for the interaction between the phase field approach for brittle fracture and the interface cohesive zone model, Computer Methods in Applied Mechanics and Engineering 321 (2017) 145 – 172. doi:https://doi.org/10.1016/j.cma.2017.04.004.
[67] B. Bourdin, C. J. Larsen, C. L. Richardson, A time-discrete model for dynamic fracture based on crack regularization, International Journal of Fracture 168 (2) (2011) 133–143. doi:10.1007/s10704-010-9562-x.
[68] G. A. Francfort, C. J. Larsen, Existence and convergence for quasi-static evolution in brittle fracture, Communications on Pure and Applied Mathematics 56 (10) (2003) 1465–1500. doi:10.1002/cpa.3039.
[69] M. J. Borden, T. J. Hughes, C. M. Landis, C. V. Verhoosel, A higher-order phase-field model for brittle fracture: Formula-

tion and analysis within the isogeometric analysis framework, Computer Methods in Applied Mechanics and Engineering 273 (2014) 100 – 118. doi:https://doi.org/10.1016/j.cma.2014.01.016.

[70] A. Braides, Gamma-convergence for beginners, in: of Oxford Lecture Series in Mathematics and its Applications, University Press, 2002.

[71] F. Iurlano, A density result for gsbd and its application to the approximation of brittle fracture energies, Calculus of Variations 51 (2014) 315–. doi:10.1007/s00526-013-0676-7.

[72] A. Chambolle, V. Crismale, Compactness and lower semicontinuity in *gsbd* (2018). arXiv:1802.03302.

[73] A. Dean, J. Reinoso, N. Jha, E. Mahdi, R. Rolfes, A phase field approach for ductile fracture of short fibre reinforced composites, Theoretical and Applied Fracture Mechanics 106 (2020) 102495. doi:https://doi.org/10.1016/j.tafmec.2020.102495.

[74] A. Dean, P. Asur Vijaya Kumar, J. Reinoso, C. Gerendt, M. Paggi, E. Mahdi, R. Rolfes, A multi phase-field fracture model for long fiber reinforced composites based on the puck theory of failure, Composite Structures 251 (2020) 112446. doi:https://doi.org/10.1016/j.compstruct.2020.112446.

[75] L. Ambrosio, V. M. Tortorelli, Approximation of functional depending on jumps by elliptic functional via γ-convergence, Communications on Pure and Applied Mathematics 43 (8) 999–1036. doi:10.1002/cpa.3160430805.

[76] L. Ambrosio, V. M. Tortorelli, On the approximation of free discontinuity problems, 1992.

[77] G. Alberti, Variational models for phase transitions, an approach via Γ-convergence, Springer Berlin Heidelberg, Berlin, Heidelberg, 2000, pp. 95–114. doi:10.1007/978-3-642-57186-2_3.

[78] L. Evans, Measure Theory and Fine Properties of Functions., 1992. doi:https://doi.org/10.1201/9780203747940.

[79] J.-Y. Wu, V. P. Nguyen, C. Thanh Nguyen, D. Sutula, S. Bordas, S. Sinaie, Phase field modelling of fracture, Advances in Applied Mechanics 53 (09 2019).

[80] R. H. J. PEERLINGS, R. DE BORST, W. A. M. BREKELMANS, J. H. P. DE VREE, Gradient enhanced damage for quasi-brittle materials, International Journal for Numerical Methods in Engineering 39 (19) (1996) 3391–3403. doi:10.1002/(SICI)1097-0207(19961015)39:19¡3391::AID-NME7¿3.0.CO;2-D.

[81] A. Simone, H. Askes, R. H. J. Peerlings, L. J. Sluys, Interpolation requirements for implicit gradient-enhanced continuum damage models, Communications in Numerical Methods in Engineering 19 (7) (2003) 563–572. doi:10.1002/cnm.597.

[82] J.-Y. Wu, Y. Huang, V. P. Nguyen, On the bfgs monolithic algorithm for the unified phase field damage theory, Computer Methods in Applied Mechanics and Engineering 360 (2020) 112704. doi:https://doi.org/10.1016/j.cma.2019.112704.
URL `http://www.sciencedirect.com/science/article/pii/S0045782519305924`

[83] P. K. Kristensen, E. Martínez-Pañeda, Phase field fracture modelling using quasi-newton methods and a new adaptive step scheme, Theoretical and Applied Fracture Mechanics 107 (2020) 102446. doi:https://doi.org/10.1016/j.tafmec.2019.102446.
URL `http://www.sciencedirect.com/science/article/pii/S0167844219305580`

[84] C. Miehe, F. Welschinger, M. Hofacker, Thermodynamically consistent phase-field models of fracture: Variational principles and multi-field fe implementations, International Journal for Numerical Methods in Engineering 83 (10) (2010) 1273–1311. doi:10.1002/nme.2861.

[85] E. M. G. G. Galvez, J., J. Planas, Crack trajectories under mixed mode and non-proportional loading., International Journal of Fracture (1996) 171–193.

[86] J.-R. Cho, Evaluation of stress intensity factors in functionally graded materials by natural element method, Journal of Mechanical Science and Technology 33 (1) (2019) 299–306. doi:10.1007/s12206-018-1229-y.

[87] F. Fantoni, A. Bacigalupo, M. Paggi, J. Reinoso, A phase field approach for damage propagation in periodic microstructured materials, International Journal of Fracture 223 (2029) 53–76.